Pergamon

Geochimica et Cosmochimica Acta, Vol. 67, No. 11, pp. 1937–1953, 2003

0016-7037/03 $30.00 + .00

doi:10.1016/S0016-7037(00)01301-7

X-ray absorption fine structure study of As(V) and Se(IV) sorption complexes on hydrous Mn oxides

ANDREA L. FOSTER,[1,*] GORDON E. BROWN, JR.,[1,2] and GEORGE A. PARKS[1]

[1]Surface and Aqueous Geochemistry Group, Department of Geological and Environmental Sciences, Stanford University, Stanford, CA 94305-2115, USA

[2]Stanford Synchrotron Radiation Laboratory, SLAC, 2575 Sand Hill Road, MS. 99, Menlo Park, CA 94025, USA

(*Received May* 22, 2001; *accepted in revised form October* 17, 2002)

Abstract—X-ray absorption fine structure (XAFS) spectroscopic analysis at the As, Se, and Mn K-edges was used to study arsenate [$As(V)O_4^{3-}$] and selenite [$Se(IV)O_3^{2-}$] sorption complexes on the synthetic hydrous manganese oxides (HMOs) vernadite (δ-MnO_2) and K-birnessite (nominal composition: $K_4Mn_{14}O_{27} \cdot 9H_2O$). No significant changes were observed in sorption complex structure as a function of sorbent, pH (5 to 8), surface coverage (0.04 to 0.73 μmol/m^2), or reaction time (5 to 22 h) in the arsenate or selenite systems. In the arsenate/HMO system, extended XAFS parameters indicate an average second-neighbor As(V) coordination of 2.0 $\pm$ 0.4 Mn at an average distance of 3.16 $\pm$ 0.01 Å, which is consistent with formation of $As(V)O_4$ sorption complexes sharing corners with two adjacent $Mn(IV)O_6$ surface species (i.e., bidentate, binuclear). In the selenite/HMO system, selenite surface complexes are surrounded by two shells of Mn atoms, which could represent two different adsorption complexes or a precipitate. The first shell consists of 1.6 $\pm$ 0.4 Mn at 3.07 $\pm$ 0.01 Å, which is consistent with the selenite anion forming bidentate (mononuclear) edge-sharing complexes with $Mn(II)O_6$ or $Mn(III)O_6$ octahedra. The second shell consists of 1.4 $\pm$ 0.4 Mn at 3.49 $\pm$ 0.03 Å, consistent with selenite forming monodentate, corner-sharing complexes with $Mn(II)O_6$ or $Mn(III)O_6$ octahedra. Pauling bond valence analysis that uses the extended XAFS-derived bond lengths for As(V)-O, Se(IV)-O, and Mn-O bonds indicates that the proposed surface complexes of selenite and arsenate on HMOs should be stable. Although a nearly identical Se(IV) coordination environment is found in a crystalline Mn(II)-Se(IV) precipitate (which has a structure similar to that of $MnSeO_3 \cdot H_2O$), there are significant differences in the X-ray absorption near-edge structure and extended XAFS spectra of this precipitate and the selenite/HMO sorption samples. These differences coupled with transmission electron microscopy results suggest that if a precipitate is present it lacks long-range order characteristic of crystalline $MnSeO_3 \cdot H_2O$. *Copyright © 2003 Elsevier Science Ltd*

1. INTRODUCTION

Sorption and heterogeneous electron-transfer reactions between hydrous manganese oxide (HMO) phases and oxoanion-forming elements such as arsenic (As), selenium (Se), molybdenum (Mo), and tungsten (W) play an important role in determining the distribution of these anions in terrestrial (Hess and Blanchar, 1976), lacustrine (Oscarson et al., 1981), and oceanic environments (Takematsu et al., 1990; Kunzendorf and Glasby, 1992). These interactions are of environmental importance in that arsenite ($(As(III)O_{3-n}(OH)_n)^{(n-3)}$, n = 0 to 3), arsenate ($(As(V)O_{4-n}(OH)_n)^{(n-3)}$, n = 0 to 3), selenite ($(Se(IV)O_{3-n}(OH)_n)^{(n-2)}$, n = 0 to 2), and selenate ($(Se(VI)O_{4-n}(OH)_n)^{(n-2)}$, n = 0 to 2) are more toxic than many of their organic and inorganic reduced forms (Mayland, 1994; Yamauchi and Fowler, 1994).

Both arsenite and selenite undergo heterogeneous oxidation by K-birnessite (type formula: $K_4Mn_{14}O_{27} \cdot 9H_2O$; McKenzie, 1989), but the half-life (τ) of the electron transfer reaction between As(III) and Mn(IV) in K-birnessite is almost four orders of magnitude faster than the electron transfer reaction between Se(IV) and Mn(IV) in K-birnessite (τ = 33 s and $10^{6.9}$ s, respectively; Scott, 1991). The reaction products (arsenate and selenate) exhibit very different sorption behavior on hydrous metal oxides. Arsenate forms relatively strong chemical bonds with hydrous metal oxide surfaces, essentially independent of net surface charge (Sadiq, 1997), suggesting dominantly inner-sphere surface complexation as verified independently by X-ray absorption fine structure (XAFS) spectroscopy (e.g., Waychunas et al., 1993). In contrast, selenate predominantly forms weak electrostatic bonds to hydrous metal oxides, and its sorption is usually surface-charge dependent (Balistrieri and Chao, 1990), suggesting dominantly outer-sphere complexation, which is consistent with some XAFS measurements (e.g., Hayes et al., 1987). The strong sorption behavior of arsenate and slow oxidation kinetics of selenite imply that these two species are likely to be the dominant As and Se species associated with HMO surfaces over long time periods under natural conditions (although HMO phases are probably not as effective as hydrous ferric oxides for oxoanion sorption; Balistrieri and Chao, 1990).

Macroscopic oxidation/sorption studies and X-ray photoelectron spectroscopy (XPS) studies have independently concluded that differences in the oxidation kinetics of Se(IV) and As(III) on K-birnessite might be due to the formation of different types of surface complexes. XPS results (Nesbitt et al., 1998) and a macroscopic sorption study using manganite [Mn(III)OOH] as the sorbent/oxidant (Chiu and Hering, 2000) demonstrate that Mn(IV) and Mn(III) can both function as

* Author to whom correspondence should be addressed, at U.S. Geological Survey, 345 Middlefield Road, MS 901, Menlo Park, CA 94025, USA (afoster@usgs.gov).

electron acceptors for arsenite. In contrast, an XPS study of Se(IV) on HMO (Banerjee and Nesbitt, 2000) suggests that Mn(III) surface sites do not participate in selenite oxidation and may even inhibit the process. These results suggest that surface Mn speciation is an important variable to consider in the redox activity of HMO surfaces.

Other studies suggest that variations in HMO structure may be important in the sorption of arsenate and selenite. For example, Takamatsu et al. (1985) determined that up to 80% of added arsenate was sorbed to amorphous manganese oxide at pH 4 after overnight equilibration, but Scott and Morgan (1995) found negligible sorption of arsenate on K-birnessite after 4 h of reaction at pH 4. However, XPS studies provide evidence for the presence of surface-bound arsenate on K-birnessite during arsenite oxidation (Nesbitt et al., 1998). In Se(IV)/HMO systems, Scott and Morgan (1996) observed heterogeneous oxidation of sorbed selenite by K-birnessite on timescales of hours to days, but Balistrieri and Chao (1990) reported no detectable selenite oxidation on amorphous manganese oxide during 24-h sorption experiments. XPS studies verify that Se(IV) is slowly oxidized to Se(VI) by K-birnessite, but also indicate that the reaction does not go to completion under the conditions studied (Banerjee and Nesbitt, 2000).

A recent extended X-ray absorption fine structure (EXAFS) study by Manning et al. (2002) compared the structure and composition of As(V) sorption complexes on K-birnessite under two conditions: (1) in the absence of As(III), and (2) as a result of heterogeneous As(III) oxidation. Both the number of neighboring Mn atoms and the As-Mn interatomic distance were nearly identical for the two conditions (approximately two neighboring Mn atoms at ~3.22 Å, respectively). These parameters are consistent with a bidentate, binuclear sorption geometry identical to the predominant type of sorption complex formed by As(V) (and Se(IV)) on hydrous ferric oxides (Hayes et al., 1987; Waychunas et al., 1993).

We have analyzed XAFS spectra at the Mn, As, and Se K-edges to determine the molecular-scale composition and structure of arsenate and selenite sorption complexes on synthetic vernadite (δ-MnO_2) and K-birnessite. This information provides new insight into the results of previous macroscopic sorption and ex situ spectroscopic studies, because in situ XAFS spectroscopic investigations can be used to constrain sorbate stoichiometry, geometric structure, and mode of attachment at oxide/aqueous solution surfaces (e.g., O'Day et al., 1996). In addition to providing new XAFS information on the Se(IV)/HMO system, this report also examines the As(V)/HMO system over a range of experimental parameters, which was not done in the Manning et al. (2002) study. Although examination of As(III) sorption/oxidation on HMO phases by standard, room-temperature XAFS spectroscopy is precluded because of the rapid rate of As(III) oxidation (Manning et al., 2002), the slow oxidation kinetics of Se(IV) coupled with the previously demonstrated low sorption affinity of Se(VI) on Mn oxides (Balistrieri and Chao, 1990) result in favorable conditions for the spectroscopic examination of Se(IV) sorption products on HMO surfaces.

Previous XAFS studies of As and Se sorption on synthetic hydrous ferric oxides have proven useful in investigations of As and Se distributions in natural systems (Foster et al., 1998b; Foster, 1999; La Force et al., 2000; Savage et al., 2000). Similarly, the results of this study should prove useful for researchers investigating As or Se in natural environments such as oceanic ferromanganese deposits (Takematsu et al., 1990; Kunzendorf and Glasby, 1992), lake sediments (Oscarson et al., 1981; Roman-Ross et al., 2001), and oxidizing, Mn oxide and arsenic-rich groundwater systems such as those in central Argentina (Smedley et al., 2001).

2. EXPERIMENTAL

2.1. Materials Preparation and Characterization

Synthetic vernadite was prepared by rapid oxidation of a 30 mM $MnCl_2$ solution with an equal volume of a 20 mM $KMnO_4$ solution at pH 10. The dried product appears black in color, and is composed of crystallite agglomerations (Fig. 1a). Reddish-brown K-birnessite was prepared by the slow acid reduction of 1.16 L of a vigorously boiling, stirred 0.2 mol/L $KMnO_4$ solution by 83.5 mL of 10 mol/L HCl, (McKenzie, 1971; Scott and Morgan, 1995). The K-birnessite has the characteristic "balls of needles" morphology (Fig. 1b). Both precipitates were washed several times with doubly deionized (DDI) water using a vacuum flask with a 0.2-μm filter, centrifuged, and resuspended in DDI water. After dialysis against DDI water for ~7 d, the precipitates were pelleted, vacuum dried, and stored in glass jars with polypropylene caps. Average surface areas of 295 ± 30 m^2/g for vernadite and 150 ± 17 m^2/g for K-birnessite were determined by multipoint Brunauer-Emmett-Teller (BET)-N_2 adsorption (n = 2 for both phases). The pH of zero net proton charge (pH_{znpc}) of K-birnessite has been estimated at 2.7 (Morgan and Stumm, 1964; Scott and Morgan, 1995), and the pH_{znpc} of vernadite is estimated to be less than 1.5 (McKenzie, 1981; Balistrieri and Murray, 1982). Mn(II)-arsenate and Mn(II)-selenite precipitates were synthesized according to the method described for Mn(II)-arsenate in Hess and Blanchar (1976). The resulting pale pink (As) and pinkish-white (Se) precipitates were rinsed, vacuum-dried, and stored in glass bottles.

Aqueous slurries of pristine HMO phases and HMOs reacted with Se(IV) or As(V) were filtered onto glass fiber filters for powder X-ray diffraction (XRD) data collection. Mn-containing precipitates were ground in an agate mortar and pestle and top-loaded into a silica glass holder for XRD data collection. Powder XRD data were collected with a Rigaku Geigerflex θ-θ diffractometer equipped with a Cu X-ray tube and a graphite monochromator over the 2θ range 5 to 65° or 5 to 80° (3 s count time/0.05 2θ step).

The main peak in the powder XRD pattern of vernadite occurs at 37.26° 2θ (d = 2.41 Å; Fig. 1c), in agreement with previously reported values (Burns and Burns 1979; Balistrieri and Chao, 1990). The XRD pattern of the synthetic K-birnessite used in this study (Fig. 1c) has a basal reflection at 12.01° 2θ (d = 7.37 Å), which is larger than the interlayer spacing of 7.1 Å determined by Post and Veblen (1990). According to Drits et al. (1997), the XRD pattern of turbostratic birnessite typically contains only the three primary reflections, which suggests that the K-birnessite used in this study is also turbostratic. XRD patterns of vernadite after reaction with As(V) and Se(IV) contain a broad, relatively weak peak at 22 to 24° 2θ (d = 4.0 to 3.6 Å; Fig. 1d) that is not present in the unreacted vernadite XRD pattern, indicating that either the synthetic vernadite is undergoing a phase transformation or that a new phase is forming during the reaction, among other possibilities. In addition, XRD patterns of vernadite after reaction with As(V) and Se(IV) were collected out to 80° 2θ and showed an additional peak at 65 to 66° 2θ (d = 1.44 to 1.41 Å); this peak coincides with the second most intense peak in synthetic vernadite (Burns and Burns 1979; Balistrieri and Chao, 1990).

An artificially broadened (crystallite diameter = 100 Å), simulated XRD pattern of geigerite $[Mn_5(H_2O)_8(AsO_3OH)_2(AsO_4)_2 \cdot 2H_2O]$ produced by CERIUS2.3 (Molecular Simulations Inc.) provided the best match to the broad reflections of the Mn(II)-arsenate precipitate XRD pattern, primarily as a result of the overlap of the basal reflection at 8.4° 2θ (d = 10.5 Å; Fig. 1e). Comparison with the calculated XRD patterns of other known Mn(II)-arsenate phases produced poorer matches.

The XRD powder pattern of the Mn(II)-selenite precipitate best matches that of $MnSeO_3 \cdot H_2O$ (Koskenlinna and Valkonen, 1977) if a preferred orientation correction along (010) is used to generate the

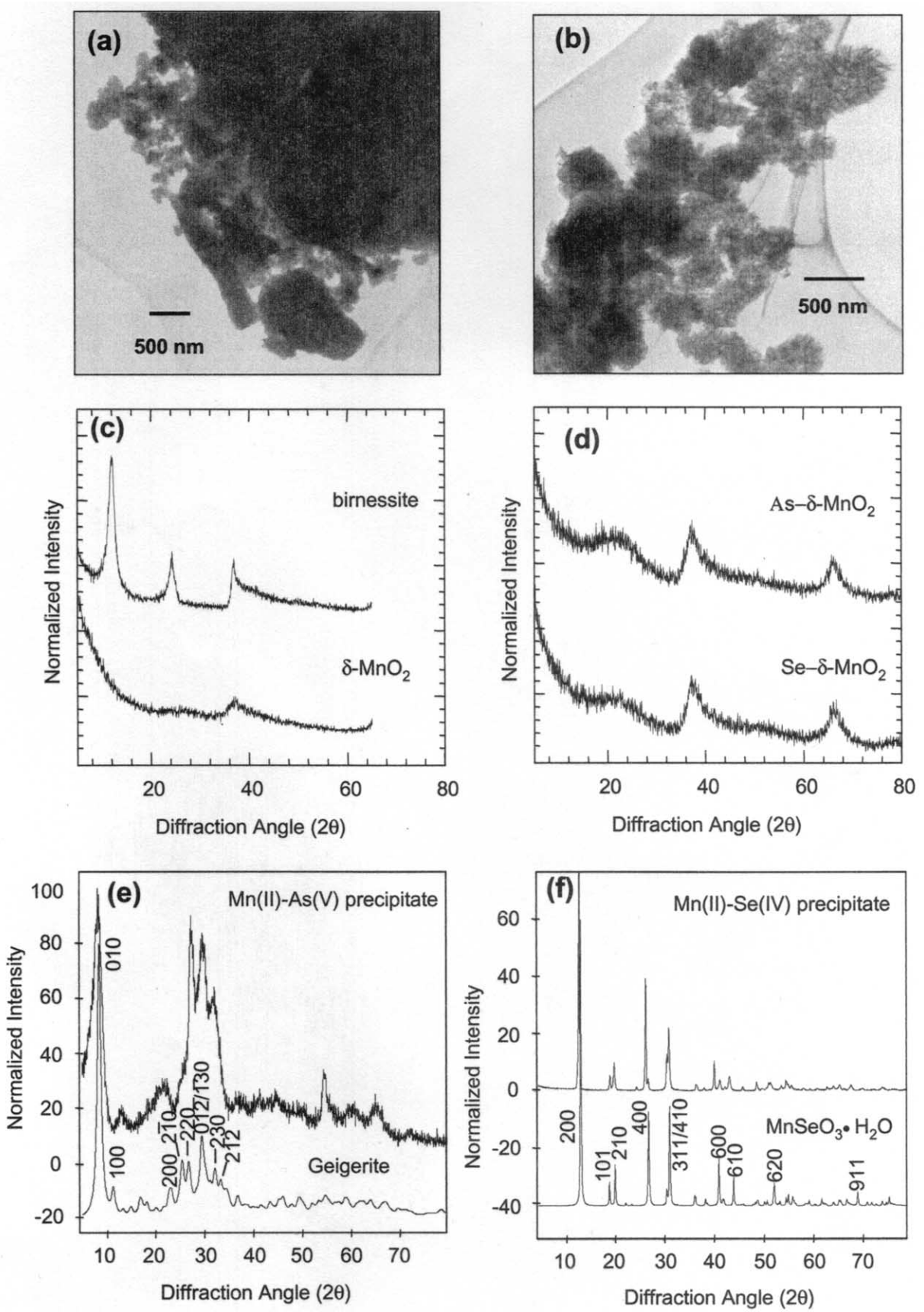

Fig. 1. TEM images of synthetic vernadite (a) and K-birnessite (b) showing differences in morphology and particle size. The K-birnessite XRD pattern (c) has few reflections, suggesting that it is turbostratic. The strongest line in the K-birnessite pattern is the basal plane reflection at 12.01° 2θ (7.37 Å), which is lacking in the pattern of δ-MnO_2 (c). After reaction with As(V) or Se(IV), a new peak at 22 to 24° 2θ is observed in the δ-MnO_2 pattern (d), but the new reflections do not match the strongest lines of known Mn(II)-oxoanion precipitates. A simulated geigerite pattern broadened using a 100 Å mean crystal diameter compares favorably with the experimental XRD pattern of the synthetic Mn(II)-As(V) precipitate (e). A simulated pattern of $MnSeO_3 \cdot H_2O$ generated using a preferred orientation correction along (010) provides a good match to the experimental XRD pattern of the synthetic Mn(II)-Se(IV) precipitate (f).

simulated XRD pattern for $MnSeO_3 \cdot H_2O$. Although the strongest lines of this simulated pattern, particularly the reflection at 13.1° 2θ (d = 6.72 Å), match the experimental pattern (Fig. 1f), some minor reflections in the experimental XRD pattern are not matched, which may indicate the presence of other phases (presumably also Mn-selenites).

2.2. Sorption Sample Preparation and Chemical Analysis

Samples of As(V) and Se(IV) sorbed to vernadite and K-birnessite were prepared by equilibrating an HMO slurry in a 0.01- or 0.1-mol/L $NaNO_3$ solution under ambient conditions (19 to 22°C) at the desired pH (5 to 8) for 1 to 4 h (Fig. 2). After equilibration, the stirred suspension was spiked with a small volume of concentrated sodium arsenate ($Na_2HAsO_4 \cdot 7H_2O$) or sodium selenite (Na_2SeO_3) solution, and the pH readjusted with HNO_3 or NaOH to the desired value. Resultant initial anion concentrations ranged between 35 to 300 μM, with solids concentration ranging from 2.5 to 5.0 g/L (Table 1). The kinetics of Se(IV) uptake on both minerals were examined under the following conditions: $[Se]_{initial}$ = 1 to 1.5 mM, [HMO] = 2.5 g/L, and pH = 4.0 ± 0.5 in continuously stirred vessels. After measurement of the final pH, the slurries were pelleted by centrifugation ($g_{average}$ = 20000, time = 20 min), except for kinetic experiments, in which 5-mL aliquots of the slurry were periodically removed. All solutions were filtered to 0.2 μM and acidified with concentrated HNO_3 before analysis.

Total dissolved As, Se, and Mn were measured with either a graphite furnace atomic absorption (GFAA) spectrophotometer (Varian SpectrAA) with deuterium background correction or a Hewlett Packard 4500 inductively coupled plasma mass spectrometer (ICP-MS) with Sc as the internal standard. GFAA or ICP-MS grade calibration standards were prepared with either 0.01 or 0.1 mol/L HNO_3. For both methods the operational detection limits were 5 μg/L and reproducibility of replicate analyses ranged between 2 and 10%. The adsorption of Se and As was calculated by the expression Γ ($\mu mol_{anion}/m^2$) = ($[Anion]_{initial}$ − $[Anion]_{final}$)/[solids], in which the concentration of the anion is in μmol/L and the solids concentration in m^2/L.

2.3. Equilibrium Thermodynamic Calculations

The activities of free Mn^{2+}, AsO_4^{3-}, and SeO_3^{2-} species were determined by the thermodynamic data in the GEOCHEM-PC 2.0 speciation code (Parker et al., 1987), and used in calculation of the saturation indices listed in Table 1. After reviewing the default thermodynamic databases of several speciation codes (MINTAQ3.11, HYDRAQL 1.0, GeochemPC 2.0, and Geochemists' Workbench 3.2) and the tabulated stability constants of Sillén and Martell (1964), we found thermodynamic data for hydrated phases such as $Mn_3(AsO_4)_2 \cdot 8H_2O$ (Gabrielson, 1951), and $MnSeO_3 \cdot 2H_2O$ (Koskenlinna et al., 1976); these phases, or others such as $Mn_2AsO_4(OH)$ (Rochette et al., 1998) are the types of solids most likely to form under the conditions of our sorption experiments. However, we used stability data for anhydrous $Mn_3(AsO_4)_2$ and $MnSeO_3$ in our calculations for several reasons: (1) the anhydrous phases are several orders of magnitude less soluble than the hydrous analogs and therefore provide a conservative estimate of the saturation state of sorption experiments; (2) the original source of the data for the hydrous phases could not be located, whereas stability data for the anhydrous phases could be validated; (3) reported log K values for the hydrous phases varied substantially between databases.

As a starting point for activity calculations, we used a total dissolved Mn concentration of 63 μM. This value is near the maximum dissolved Mn measured in kinetic uptake experiments at pH 4 (see section 4.1) and was used because dissolved Mn concentrations were not measured on the same sorption samples from which EXAFS data were collected. However, for calculation of $Mn_3(AsO_4)_2$ and $MnSeO_3$ stability diagrams, the activity of Mn^{2+} was assumed to equal the total dissolved Mn concentration. This is a reasonable assumption at pH 5, but is probably an overestimate of $[Mn^{2+}]$ at pH 8. Stability diagrams (Fig. 3) were prepared by Geochemists' Workbench 3.0 (RockWare Software) using its default thermodynamic database (pertinent data did not differ from that in the GEOCHEM-PC2.0 database).

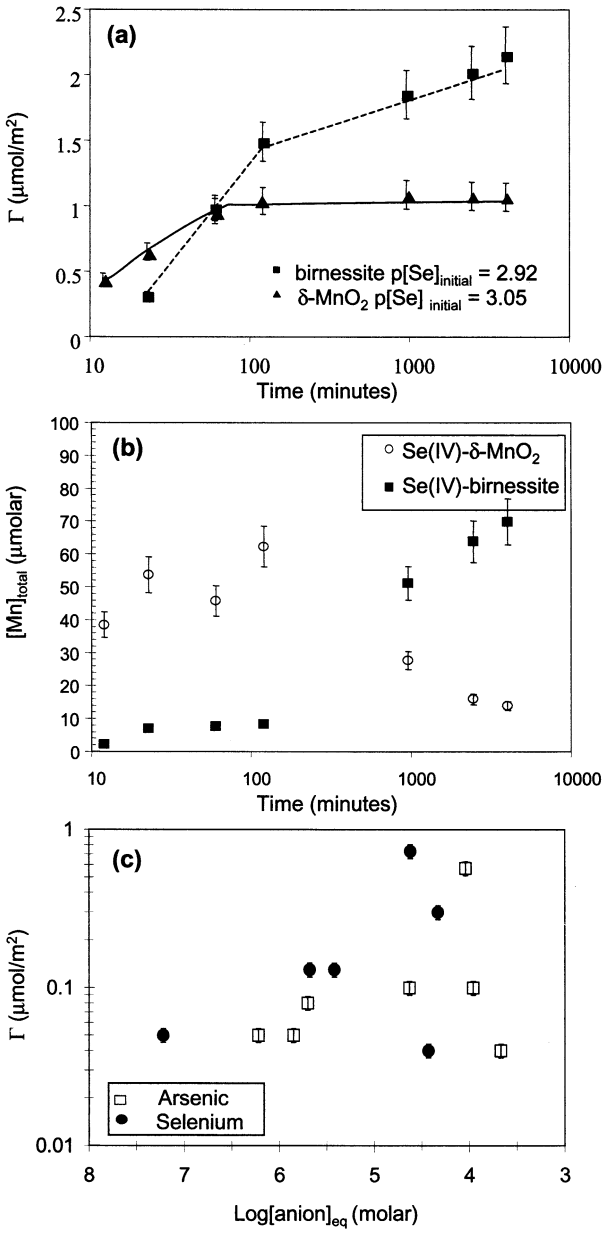

Fig. 2. (a) Uptake of Se(IV) on K-birnessite (dotted line) and δ-MnO_2 (solid line) as a function of time at pH = 4.0 ± 0.5 (lines are visual guides, not fits). (b) Dissolved Mn concentration as a function of time in the uptake experiments shown in (a). (c) Se(IV) and As(V) uptake in batch sorption experiments on vernadite and K-birnessite, plotted as a function of the final concentration, in molar units (note log scale). Ten percent error bars are shown in each panel. Data points plotted in (c) represent individual samples prepared under different conditions of pH, initial anion concentration, solids concentration, and equilibration time, and as such do not constitute sorption isotherms.

2.4. XAFS Data Collection and Analysis

Pristine HMOs, reacted HMOs, and Mn-oxoanion precipitates were vacuum dried, diluted with reagent-grade boron nitride (resulting in an absorption length of 1 to 1.5), then loaded into 1.5 mm thick aluminum holders with 2 μm thick Mylar windows. Sorption samples were pelleted by centrifuge, and within 4 to 8 h the moist pellets were loaded

Table 1. Summary of EXAFS sorption sample preparation conditions. All samples were prepared in 0.01 M $NaNO_3$ except for sample SM1-1, which was prepared in 0.1 M $NaNO_3$. "A" refers to arsenate samples and "S" refers to selenite samples.

Sample	pH	Time (min)	[solids] (g/l)	p[anion] inital[a]	p[anion] final	pa_{anion}[b]	pa_{Mn2+}	SI[c]	Γ (μmol/m^2)
AM01-1[d]	8.0	600	5.40	3.57	3.67	7.37	4.35	+0.925	0.04
AM01-2	4.8	600	4.67	4.15	5.85	13.0	4.18	−9.85	0.05
AM01-3	5.4	600	5.42	3.57	3.96	11.2	4.19	−6.34	0.10
AM01-4	5.4	1050	2.50	4.01	4.63	11.7	4.19	−7.21	0.10
AM01-5	4.6	1055	2.52	4.46	6.22	13.7	4.18	−11.3	0.05
AB01-1[e]	4.7	360	2.40	4.52	5.70	13.6	4.18	−11.0	0.08
AB01-2	4.7	360	2.42	3.52	4.04	12.6	4.19	−8.99	0.57
SM01-1	5.1	300	2.40	4.02	5.68	7.47	4.18	−4.39	0.13
SM01-2	7.1	1320	4.96	4.01	4.43	5.52	4.22	−2.47	0.04
SM01-3	5.2	1065	2.49	3.57	4.33	6.92	4.19	−4.92	0.30
SM01-4	5.0	1085	2.51	4.46	7.22	8.01	4.18	−3.84	0.05
SM1-1	5.0	330	2.40	4.02	5.42	7.57	4.18	−4.49	0.13
SB01-1	4.6	360	2.42	3.52	4.62	7.48	4.18	−4.39	0.73

[a] p[anion] = −log[anion].

[b] $pa_{anion} = -\log a_{anion}$. Activities were calculated using initial reaction conditions and thermodynamic parameters in the chemical speciation program GEOCHEM-PC 2.0 (Parker et al., 1987).

[c] SI = log (IAP/K_{SO}) for $Mn_3(AsO_4)_2$(c) or $MnSeO_3$(c) calculated using the tabulated activities of AsO_4^{3-}, SeO_3^{2-}, and Mn^{2+}, and K_{SO} values from the GEOCHEMPC database.

[d] M = synthetic vernadite.

[e] B = synthetic K-birnessite.

into 2 to 3 mm thick Teflon cells with 2 μm thick Mylar windows for XAFS data collection.

Manganese, As, and Se K-edge XAFS spectra were collected at the Stanford Synchrotron Radiation Laboratory (SSRL) on wiggler beamline IV-3, under conditions described in previous reports (Foster et al., 1998a,b). Manganese XAFS spectra were collected over the energy range 6311 to 7307 eV, As XAFS spectra were collected over the energy range 11635 to 12882 eV, and Se XAFS spectra were collected over the energy range 12435 to 13420 eV. In the vernadite systems, high-resolution Mn, As, and Se K-edge X-ray absorption near-edge structure (XANES) and extended XAFS (EXAFS) spectra were collected using Si(220) monochromator crystals as described for As and Se in previous reports (Foster et al., 1998a,b; Foster, 1999). However, for some of the vernadite and all of the K-birnessite sorption samples, lower resolution XANES spectra were obtained, because only Si(111) monochromator crystals were available at the time these data were collected. However, the energy resolution of Si(111) monochromator crystals is adequate for collection of EXAFS spectra. The absorption edge of each spectrum was calibrated to that of its respective zero-valent elemental foil (Mn: 6539.0 eV; As: 11867.0 eV, and Se: 12658.0 eV). All XAFS spectra were collected under ambient conditions (~20°C and 1 bar). Mn-XAFS spectra of the HMO phases and XAFS spectra of Mn(II)-anion precipitates were collected in transmission mode, whereas XAFS spectra of Se and As sorption samples and reacted HMO precipitates were collected in fluorescence mode using an Ar-filled Lytle detector with a 3-μm-thick (Z-1) filter and one to four layers of Al foil to reduce unwanted X-ray fluorescence as well as scattered radiation.

Details of the EXAFS data analysis methods used in this study have previously been reported (Foster et al., 1998a,b). E_o was arbitrarily chosen to be 6550 eV for Mn, 11885 eV for As, and 12675 eV for Se; ΔE_o, the difference between E_o(observed) and E_o(fit), was determined for the first shell only (i.e., Mn-O, As-O, or Se-O) and ΔE_o values for subsequent shells were assumed to be equivalent to the first shell value. Fourier transforms (FT) of the background-subtracted, $\mathbf{k}^3$-weighted EXAFS spectra were calculated over a typical $\Delta\mathbf{k}$ range of 10 to 11 Å^{-1} with a Hanning window with 0.1 width gaussian wings and 512 equally spaced points in **k**-space (EXAFSPAK; George and Pickering, 1992) or a Bessel function with window parameter = 3 and 2048 points in **k**-space (WinXAS; Ressler, 1998). Fourier transforms plotted in Figures 4d , 5b, 6c, 8c, 9a, 9b, and 10b are not corrected for phase shift (ncps); therefore, the true distances are 0.3 to 0.5 Å longer than the FT distances shown. For detailed analysis of atomic neighbors beyond the nearest oxygen atoms, FT peaks were back Fourier transformed to produce Fourier-filtered EXAFS spectra composed only of the scattering contributions from more distant atoms. The parameters derived from Fourier-filtered fits were then used as initial parameters in fits to the normalized, $\mathbf{k}^3$-weighted EXAFS spectrum (details are given below).

Theoretical backscattering phase shift and amplitude functions used in fits were generated by the computer code FEFF7 (Zabinsky et al., 1995) and the reported structures of krautite ($Mn(H_2O)(AsO_3OH)$) (Catti and Franchini-Angela, 1979), geigerite ($Mn_5(H_2O)_8(AsO_3OH)_2(AsO_4)_2 \cdot 2H_2O$ (Graeser et al., 1989), $MnSeO_3 \cdot H_2O$ (Koskenlinna and Valkonen, 1977), K-birnessite (Post and Veblen, 1990), and todorokite (Post and Bish, 1988). FEFF7 was also used to evaluate the importance of multiple scattering (MS) contributions to the EXAFS spectra of the synthetic Mn(II)-oxoanion precipitates by evaluating MS in the structures of $MnSeO_3 \cdot H_2O$ and geigerite. For this purpose, all three-leg and four-leg MS paths with a total length <3.5 Å were considered on the basis of previous studies of MS in oxoanions (Pandya, 1994; Foster, 1999). The Levenberg-Marquardt nonlinear, least-squares algorithm in EXAFSPAK and WinXAS was used to fit both Fourier-filtered and unfiltered EXAFS spectra. When fitting Fourier-filtered EXAFS spectra, the number of variable parameters was not allowed to exceed the total degrees of freedom (N_{tot}), given by the Nyquist-Brillouin relationship $N_{tot} = 2\Delta\mathbf{k}\Delta R/\pi$ (Teo, 1986; Stern, 1993); N_{tot} ranged from 6 to 9 in our fits to background-subtracted, normalized, and $\mathbf{k}^3$-weighted EXAFS spectra. Fits by the EXAFSPAK data analysis package were within the $\pm 3\sigma$ (i.e., a 99.7% confidence level) of those obtained from WinXAS, where σ is the estimated standard deviation of a fit parameter derived from the variance-covariance matrix for the raw, unsmoothed EXAFS data, as described in the EXAFSPAK manual (George and Pickering, 1992), so only EXAFSPAK fits are reported. The fits reported in Tables 2, 3, and 4 are all to $\mathbf{k}^3$-weighted, background-subtracted, normalized EXAFS spectra.

3. RESULTS AND DISCUSSION

3.1. Macroscopic Uptake and Saturation State of Sorption Experiments

In kinetic experiments, the sorption of selenite on vernadite reached a maximum at a coverage of ~1 μmol/m^2 after approximately 1.6 h, but selenite uptake on K-birnessite continued to increase until the termination of the reaction at ~27 h

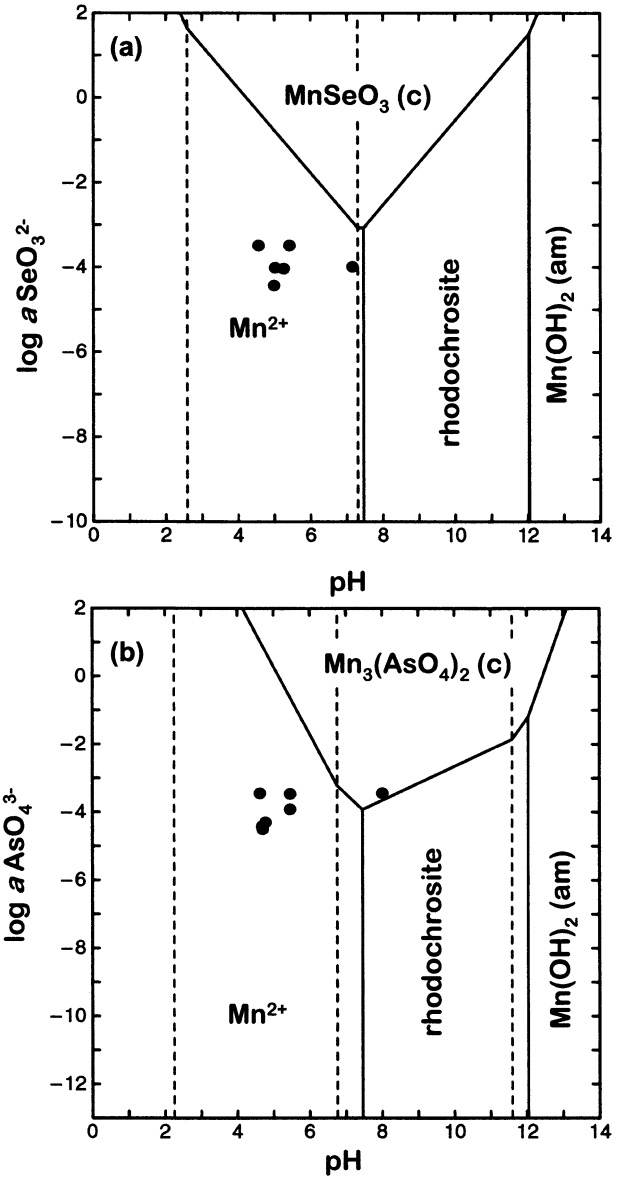

Fig. 3. Stability diagrams of anhydrous $MnSeO_3$ (a) and $Mn_3(AsO_4)_2$ (b), calculated for ambient conditions (25°C, 1 bar), and equilibrium with atmospheric CO_2(g). Total dissolved Mn concentration is $10^{-4.2}$ M. Black circles in (a) and (b) are the initial solution conditions of Se and As sorption experiments, respectively; they indicate that most experiments are predicted to be undersaturated with respect to these phases. Dashed lines in (a) and (b) indicate predominance zones for the variably protonated forms of the oxoanions.

(~2.0 μmol/m^2; Fig. 2a). The concentration of dissolved Mn was initially high ([Mn] ~$10^{-4.2}$ M) in the Se(IV)/vernadite kinetic experiment, then gradually decreased (Fig. 2b). This trend is just opposite to that observed in the Se(IV)/K-birnessite experiment. Dissolved Mn present at the onset of reaction with selenium may be derived from the proton-promoted dissolution of the HMOs during the solids equilibration step, which has been documented previously for K-birnessite (Banerjee and Nesbitt, 2000). Mn(II)-oxides and hydroxides are much more soluble than Mn(III)- or Mn(IV)-oxides and hydroxides, so the dissolved Mn is most likely Mn(II) (Banerjee and Nesbitt, 2000).

Sorption densities (Γ) attained in arsenate and selenite sorption (not kinetic) experiments on HMO vary over about an order of magnitude (0.04 to 0.73 μmol/m^2), reflecting differences in initial anion concentration, pH, and equilibration time (Fig. 2c, Table 1). By use of Balistrieri and Chao's (1990) estimate of 2.9 mol anion-active sites per kg δ-MnO_2 (calculated as one third of the total tritium-exchangeable sites) and Scott's (1991) estimate of 0.8 mol anion-active sites per kg of K-birnessite (calculated as one third of the total exchangeable site density measured by back-titration), we estimate that in our experiments adsorbed selenite occupies ≤13% and adsorbed arsenate occupies ≤10% of the anion-active sorption sites on the HMOs studied.

Although we did not monitor the production of dissolved selenate directly, the small amount of selenate produced during the sorption experiments should not significantly affect the XAFS analysis of Se(IV)/HMO sorption samples for the following reasons. First, as mentioned previously, selenite oxidation by HMOs is slow ($\tau = 10^{6.9}$s), and therefore, the amount produced over the course of our experiments (22 h maximum) should be small. Scott (1991) observed the appearance of selenate in solution only after ~12 h in oxidation experiments on K-birnessite at pH = 4, and experiments at higher pH resulted in a longer delay in the appearance of dissolved selenate. Second, selenate should not adsorb significantly to HMO surfaces under our experimental conditions because of the strongly electrostatic character of selenate sorption and the net negative charge of HMO surfaces above pH 3 (Balistrieri and Chao, 1990). Third, Se-XAFS analysis is not very sensitive to species comprising roughly 5 to 10% or less of the total sorbed Se, and selenate was below detection in all but one of our XAFS samples (which was excluded from analysis). An XPS study by Banerjee and Nesbitt (2000) demonstrated that a small amount of selenate (not quantified) was sorbed to K-birnessite along with selenite after 1.5 and 5 h of reaction, but no selenate was detected on K-birnessite surfaces after ~10 h.

Aqueous As, Se, and Mn activities were estimated from concentrations measured in uptake experiments, taking into account the formation of aqueous complexes of Mn(II)-arsenate or Mn(II)-selenite, aqueous Mn(II) complexes, and equilibrium between atmospheric and dissolved CO_2 (g). Redox reactions were not considered. According to these calculations, the solutions in selenite sorption experiments are undersaturated with respect to $MnSeO_3$ (Fig. 3a, Table 1), and with the exception of one experiment (AM01 to 1; Table 1), the solutions in arsenate sorption experiments are undersaturated with respect to $Mn_3(AsO_4)_2$ (Fig. 3b). These estimates concur with transmission electron microscopy (TEM) analysis of reacted HMO samples (not shown), in which no evidence of Mn(II) precipitates of arsenate and selenite was found.

The log K value of $Mn_3(AsO_4)_2$ reported in the GEOCHEM-PC 2.0 database is −29.6, which is close to the −28.72 value reported by Chuklantsev in 1956 (see Sillén and Martell, 1964), but much lower than the -33.7 ± 0.6 value reported for this phase in Hess and Blanchar (1976), whose recipe was followed for the synthesis of Mn(II)-arsenate. We consider the Hess and Blanchar (1976) solubility product doubtful because it was calculated on the basis of the assumption of redox

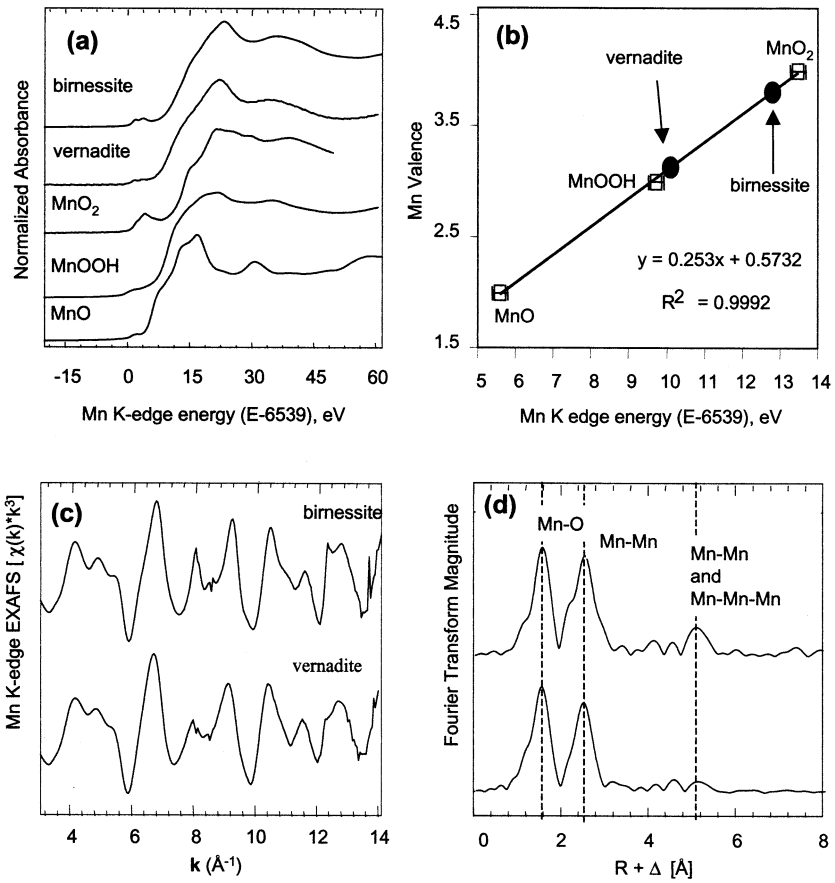

Fig. 4. (a) Mn K-edge XANES spectra of model materials and HMO phases. A calibration curve (b) was prepared by fitting a polynomial to the inflection points of three model XANES spectra (open squares), each of which was assumed to be a pure representative of a single oxidation state. Error bars of 0.2 eV are plotted for the model compounds. The strong similarity between the Mn K-edge $\mathbf{k}^3$-weighted EXAFS spectra (c) and FTs (d) of K-birnessite and vernadite reflect similarities in the local atomic structure of the two phases out to ~3 Å.

equilibrium among Mn-containing solids, which were assumed to be the products of incongruent dissolution of the $Mn_3(AsO_4)_2$ phase. If the solubility product is recalculated from Hess and Blanchar's (1976) data set without this assumption, the resulting log $K_{so} = -28.9 \pm 0.4$ agrees fairly well with Chuklantsev's value and the values in the GEOCHEM-PC 2.0 and Geochemists' Workbench databases.

3.2. Characterization of Manganese Oxide Phases and Mn(II)-Oxoanion Precipitates

Structural information for X-ray amorphous or poorly crystalline HMO phases is difficult to obtain from powder XRD patterns (see section 3.1 and Fig. 1c) because of small crystallite size, nanometer-scale phase mixing, structural/compositional impurities, and lack of material suitable for high-quality structure refinement (Turner and Buseck, 1979; Post and Veblen, 1990; Fritsch et al., 1997). Of the two HMOs used in this study, the structure of K-birnessite is better understood than the structure of synthetic vernadite. K-birnessite is a phyllomanganate composed of sheets of edge-sharing Mn(IV) octahedra, whereas vernadite is probably a compositionally variable structural intermediate between phyllomanganate and tectomanganate end-members (Chukhrov et al., 1987; Manceau et al., 1992a); tectomanganates have a higher proportion of corner-sharing octahedra than phyllomanganates (Post and Bish, 1988).

The bulk oxidation states of Mn in synthetic K-birnessite and vernadite are 3.8 and 3.1, respectively, on the basis of a calibration curve calculated by using the energy position of the first inflection point of the main edge (measured on the 1 eV smoothed first derivative spectrum) of model Mn-oxide and Mn-oxyhydroxide XANES spectra (Figs. 4a,b). The bulk Mn oxidation state of our synthetic K-birnessite is similar to values obtained in previous characterizations of the bulk and surface Mn oxidation state of this phase (Post and Veblen, 1990; Nesbitt et al., 1998; Ressler et al., 1999), and indicates that as much as 30% of the Mn in unreacted K-birnessite is present as a combination of Mn(II) and Mn(III). In contrast, the bulk Mn oxidation state of synthetic vernadite is significantly lower than that of birnessite, and indicates that under our synthesis conditions as much as 40 to 50% of the bulk Mn could be present as Mn(II).

Despite the compositional differences described above and the structural differences between vernadite and K-birnessite

Table 2. Results of least-squares analysis of Mn-EXAFS spectra. N = coordination number, R = interatomic distance, and σ = the root of σ^2, the Debye-Waller mean-square disorder parameter. The estimated standard deviations reported in parentheses following the values of each variable are 3σ and refer to the estimated error in the last decimal place, unless otherwise indicated.

	EXAFS least-squares fit results										
EXAFS samples	χ^{2a}	ΔE_o(eV)	N	R (Å)	σ (Å)	N	R (Å)	σ (Å)	N	R (Å)	σ (Å)
HMO phases			Mn-O			Mn-Mn(edge-linked)			Mn-Mn(corner-linked)		
K-birnessite	458	−3.9 (5)	6*[b]	1.90 (1)	0.07 (2)	5 (1)	2.87 (4)	0.08 (2)			
δ-MnO_2	37	−3.2 (5)	6*	1.90 (1)	0.07 (2)	4.9 (9)	2.88 (3)	0.08 (1)	0.6 (1.0)	3.47 (3)	**[c]
K-Birnessite[d] (XRD)			6	1.94		6	2.91		4	4.98	
Todorokite[e] (XRD)			6	1.89		4	2.90		4	3.51	
Mn(II)-As(V) phases			Mn-O				Mn-Mn			Mn-As	
Mn(II)-As(V) ppt.	41	6 (2)	6*	2.16 (2)	0.089 (6)	1.3 (7)	3.25 (2)	0.10 (2)	1.4 (1.0)	3.43	**
Geigerite (XRD)[f]			6	2.19		0.3	3.12		1	3.42	
						0.7	3.24		2	3.48	
						0.3	3.39		1	3.56	
						0.6	4.68		0.3	4.42	
									0.3	4.75	
Mn(II)-Se(IV) phases			Mn-O				Mn-Se			Mn-Mn	
Mn(II)-Se(IV) ppt.	45	−4.8 (1.8)	6*	2.17 (1)	0.110 (7)	1*	3.07 (01)	.054 (9)	4*	3.85 (4)	.10 (5)
									1*	4.38 (2)	.09 (2)
$MnSeO_3 \cdot H_2O$ (XRD)			6	2.20		1	3.06		4	3.85	
						2	3.42				
						1	3.62				
						1	4.38				

[a] The normalized fit error, $\chi^2 = [(\chi\text{obs} - \chi\text{calc})/\chi\text{obs}]2$.
[b] The asterisk indicates that this value was fixed in fits.
[c] The double asterisk indicates that the value was constrained to that of the previous shell.
[d] Post and Veblen, 1990.
[e] Local environment of corner-sharing Mn in todorokite only; the average bulk Mn will have fewer corner-sharing neighbors (Post and Bish, 1988).
[f] Average of three unique Mn positions.

indicated by XRD, Mn K-edge EXAFS (Mn-EXAFS) analysis suggests that the local structure around Mn in the two phases is nearly identical least out to ~3 Å. Mn K-edge EXAFS spectra and Fourier Transforms (FTs) of K-birnessite and vernadite are plotted in Figures 4c,d, and the results of nonlinear, least-squares fits to the first two atomic shells only (not shown) are summarized in Table 2. The dominant FT peak in K-birnessite and vernadite at 1.5 Å (ncps) is due to scattering from 6 O

Table 3. Results of least-squares analysis of As-EXAFS spectra. N = coordination number, R = interatomic distance, and σ = the root of σ^2, the Debye-Waller mean-square disorder parameter. The estimated standard deviations reported in parentheses following the values of each variable are 3σ and refer to the estimated error in the last decimal place unless otherwise indicated.

EXAFS samples	EXAFS least-squares fit results											
Sorption samples[a]			As-O			As-Mn			As-MS[b]		As-As	
As(V)-vernadite	χ^{2c}	ΔE_o (eV)	N	R (Å)	σ (Å)	N	R (Å)	σ (Å)	N	R (Å)	N	R (Å)
AM01-1	194	−2.4 (1.5)	5.4 (4)	1.69 (1)	.05 (2)	2.2 (4)	3.18 (1)	.063*[d]				
AM01-2	448	−2.1 (2.4)	5.2 (7)	1.70 (1)	.05 (3)	2.1 (6)	3.16 (2)	.063*				
AM01-3	149	−2.4 (1.3)	5.1 (4)	1.69 (1)	.04 (2)	1.9 (3)	3.15 (1)	.063*				
AM01-4	203	−6.7 (2.2)	6.4 (8)	1.68 (1)	.06 (3)	2.0 (5)	3.15 (2)	.063*				
AM01-5	144	−5.3 (1.6)	5.9 (5)	1.70 (1)	.06 (3)	1.7 (3)	3.16 (1)	.063*				
As(V)-K-birnessite												
AB01-1	323	−2.5 (1.8)	6.4 (6)	1.71 (1)	.06 (3)	2.2 (.5)	3.18 (1)	.063*				
AB01-2	409	−4.5 (2.2)	5.6 (6)	1.69 (1)	.05 (3)	2.0 (5)	3.16 (2)	.063*				
Model Compounds												
Mn(II)-As(V) precipitate	177	−6.5 (1.7)		1.68 (1)	.03 (2)	6.6 (1.7)	3.45 (3)	.10 (8)	15 (6)	3.10 (2)		
Geigerite[e] (XRD/FEFF)			4	1.69		4	3.46		16	3.15		
						1.5	3.56				1	3.42
						0.7	4.68				2	3.48
											0.3	4.42
											0.3	4.75

[a] A = arsenic, M = vernadite, B = K-birnessite, "01" = 0.01 M $NaNO_3$.
[b] The σ value was fixed at 0.
[c] The normalized fit error, $\chi^2 = [(\chi_{obs} - \chi_{calc})/\chi_{obs}]^2$.
[d] This value was fixed in the fit.
[e] Graeser et al. (1989); average of 2 unique As positions. FEFF7 was used to calculate multiple scattering (MS) paths as described in the text.

Table 4. Results of least-squares analysis of Se-EXAFS spectra. N = coordination number, R = interatomic distance, and σ = the root of σ^2, the Debye-Waller mean-square disorder parameter. The estimated standard deviations reported in parentheses following the values of each variable are 3σ and refer to the estimated error in the last decimal place unless otherwise indicated.

EXAFS samples	EXAFS least-squares fit results												
Sorption samples[a]			Se-O			Se-Mn1[b]			Se-Mn2[b]			Se-MS[c]	
Se(IV)-Vernadite	χ^{2d}	ΔE_o	N	R (Å)	σ (Å)	N	R (Å)	σ (Å)	N	R (Å)	σ (Å)	N	R (Å)
SM01-1	87	3.4 (1.4)	4.5 (3)	1.71 (1)	.06 (2)	1.5 (3)	3.07 (1)	.05*[e]	1.6 (5)	3.48 (2)	.06*		
SM01-2	237	6.6 (2.4)	3.6 (6)	1.73 (1)	.05 (4)	1.9 (7)	3.08 (2)	.05*	2.3 (1)	3.49 (3)	.06*		
SM01-3	63	4.4 (1.6)	4.2 (3)	1.71 (1)	.06 (2)	1.6 (2)	3.07 (1)	.05*	1.2 (4)	3.48 (2)	.06*		
SM01-4	122	4.4 (2.5)	4.2 (7)	1.70 (1)	.07 (4)	2.0 (4)	3.06 (2)	.05*	0.7 (8)	3.50 (7)	.06*		
SM1-1	73	3.7 (1.5)	4.0 (3)	1.71 (1)	.06 (2)	1.6 (3)	3.07 (1)	.05*	1.4 (5)	3.48 (2)	.06*		
Se(IV)-K-birnessite													
SB01-1	50	1.7 (1.6)	4.4 (3)	1.71 (1)	.07 (2)	1.1 (2)	3.07 (1)	.05*	1.2 (4)	3.49 (2)	.06*		
Model Compounds													
Mn(II)-selenite	46	3.7 (1.1)	4.6 (3)	1.70 (1)	.05 (2)	1*	3.03 (1)	.05 (04)	2*	3.42 (1)	.06 (3)	39 (2)	3.22 (2)
$Mn(II)SeO_3 \cdot H_2O$[f]			3	1.70		1	3.06		2	3.42		13	3.22
$Mn(III)_2(SeO_3)_3 \cdot 3H_2O$[g]			3	1.72		3	3.22		0.7	3.74			

[a] S = selenium, M = vernadite, B = birnessite; "01" and "1" refer to 0.01 and 0.1 M $NaNO_3$, respectively.
[b] The σ value was fixed to the value of the analogous shell in $MnSeO_3 \cdot H_2O$.
[c] The σ value was set at zero.
[d] The normalized fit error, $\chi^2 = [(\chi_{obs} - \chi_{calc})/\chi_{obs}]^2$.
[e] The asterisk indicates a value fixed in the fit.
[f] Koskenlinna and Valkonen (1977b); using reported structure of this compound, FEFF7 was used to calculate multiple scattering (MS) paths as described in the text.
[g] Koskenlinna and Valkonen (1977a); average of three unique Se positions.

atoms (interatomic distance, $R_{Mn\text{-}O} = 1.90 \pm 0.01$ Å in both phases), and the second peak at 2.5 Å(ncps) arises from scattering by Mn atoms (~5 Mn at 2.87 ± 0.04 Å in both phases). These first- and second-shell fit results are similar to those obtained in previous EXAFS studies of synthetic K-birnessite (Ressler et al., 1999) and vernadite (Manceau et al., 1992b). Although Mn-O bond distances generally increase with decreasing Mn oxidation state (Shannon, 1976), the EXAFS-derived Mn-O distances in birnessite and vernadite are the same within error, which does not reflect the more reduced Mn in the latter, as indicated by XANES data. This similarity may be due to the compensating effects of: (1) the higher proportion of corner-sharing vs. edge-sharing MnO_6 octahedra in vernadite (Manceau et al., 1992a,b), which should favor shorter Mn-O distances in this phase, and (2) the lower average oxidation state of Mn in the synthetic vernadite used in this study.

In this study, however, we do not find conclusive evidence that our synthetic vernadite contains more corner-sharing MnO_6 octahedra than K-birnessite. Although Manceau et al. (1992b) state that the small but important peak at 3.0 Å in the FT of vernadite (ncps) is derived from single-scattering off of second-neighbor Mn in corner-shared MnO_6 octahedra, the amplitude of this peak appears to be greater in our synthetic K-birnessite than in our synthetic vernadite. Additional evidence for or against the corner-sharing hypothesis might be provided by the FT peak at 5.1 Å (ncps), which has less amplitude in the vernadite FT than in the K-birnessite FT (Fig. 4d). This peak has previously been identified as a combination of Mn-Mn and Mn-Mn-Mn photoelectron multiple scattering paths, with the latter dominating the peak intensity (Ressler et al., 1999). Because the amplitude of the Mn-Mn-Mn scattering path is sensitive to deviations from linear alignment of the three Mn atoms (Ressler et al., 1999), it therefore should be strongest within minimally distorted sheets of edge-sharing MnO_6 octahedra. This peak is most intense in the K-birnessite FT, suggesting that K-birnessite has more ordered sheets of edge-sharing MnO_6 octahedra and/or a greater proportion of edge-sharing MnO_6 octahedra than the vernadite used in this study.

The coordination environment of Mn in the Mn(II)-arsenate precipitate is similar to that of geigerite, confirming the interpretation of XRD powder patterns (top spectrum and FT in Figs. 5a,b, respectively; also see section 3.1 and Fig. 2e). Geigerite has a framework structure composed of edge-sharing MnO_6 octahedra bonded to $As(V)O_4$ tetrahedra through corners (Graeser et al., 1989). Mn-EXAFS analysis indicates an average interatomic distance ($R_{Mn\text{-}O}$) of 2.16 ± 0.01 Å, consistent with the average $R_{Mn(II)\text{-}O}$ reported for geigerite (Table 2). The remainder of the local coordination environment contains ~1.3

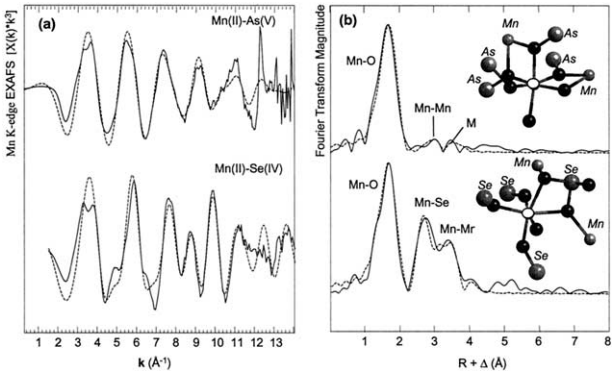

Fig. 5. Mn K-edge $\mathbf{k}^3$-weighted EXAFS spectra (a) and FTs (b) of Mn(II)-oxoanion precipitates. Dashed lines in (a) and (b) are the result of least-squares fits to the $\mathbf{k}^3$-weighted EXAFS spectra. The Mn local structure in the Mn(II)-As(V) precipitate is very similar to the reported structure of geigerite (b, top), if the two unique Mn positions are averaged. The Mn local structure in the Mn(II)-Se(IV) precipitate is very similar to the reported structure of $MnSeO_3 \cdot H_2O$ (b, bottom). The white circle in both graphics represents a central absorbing Mn atom.

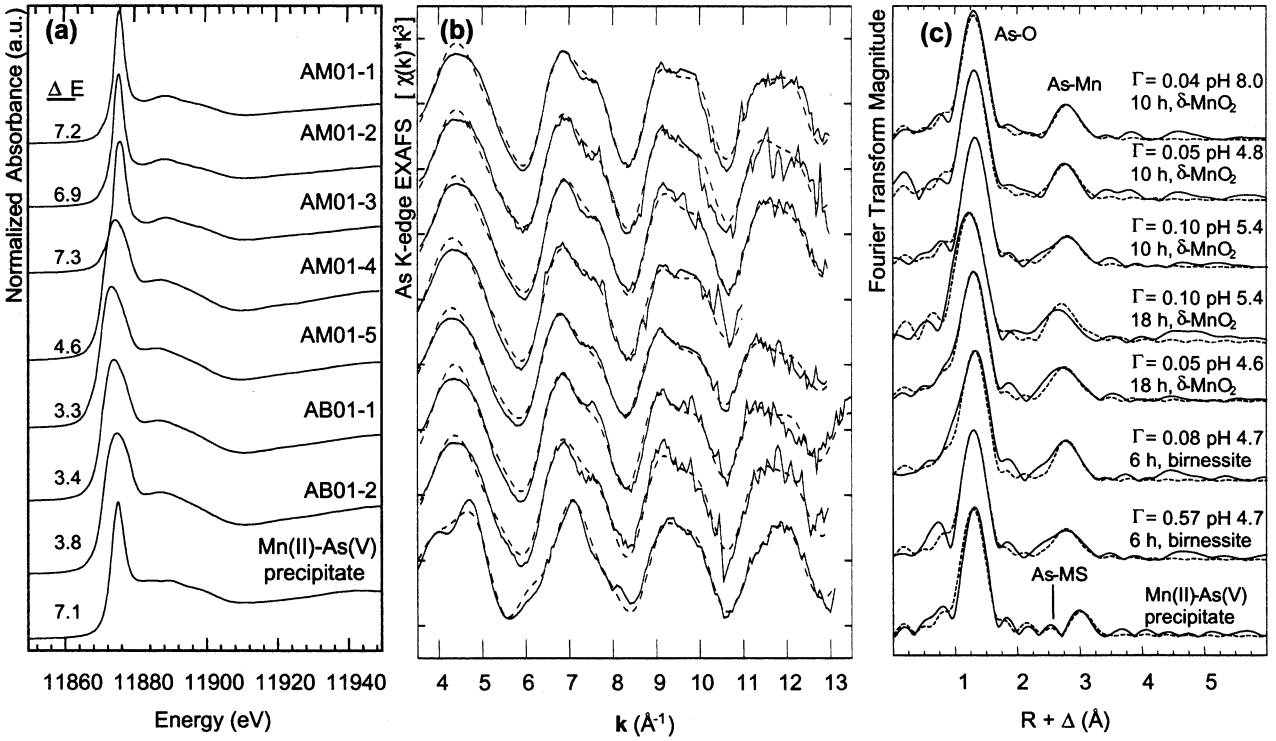

Fig. 6. (a) Normalized As K-edge XANES spectra of HMO sorption samples and the Mn(II)-As(V) precipitate; ΔE is the energy difference between the absorption edge position of samples/precipitates and the elemental arsenic absorption edge at 11867.0 eV. XANES spectra of AM01-4, AM01-5, AB01-1, and AB01-2 were collected under low-resolution conditions and therefore have different ΔE values. (b) Arsenic K-edge EXAFS spectra and (c) Fourier transforms (solid lines) of As(V) sorbed to vernadite and K-birnessite and the Mn(II)-As(V) precipitate. Nonlinear, least-squares fits to $\mathbf{k}^3$-weighted EXAFS spectra are plotted as dotted lines. Sorption sample spectra appear very similar to one another but are distinct from the model precipitate.

Mn at 3.25 ± 0.02 Å and ~1.4 As at 3.43 ± 0.02 Å, which is in agreement with the reported Mn coordination in geigerite if the two unique atomic positions of Mn are averaged.

Mn-EXAFS of the Mn(II)-selenite precipitate indicates that the local structure around Mn is similar to that in $MnSeO_3 \cdot H_2O$, which is also consistent with our interpretation of XRD powder patterns (bottom spectrum and FT in Figs. 5a,b, respectively; see also section 3.1, Fig. 2f). The least-squares fit to the Mn-EXAFS spectrum consists of an average R_{Mn-O} of 2.17 ± 0.01 Å, which is similar to that reported in the $MnSeO_3 \cdot H_2O$ structure (Table 2). Additional parameters derived from the fit (~1 Se at 3.07 ± 0.01 Å, ~4 Mn at 3.85 ± 0.04Å, and ~1 Se at 4.38 ± 0.02 Å) are also in agreement with the $MnSeO_3 \cdot H_2O$ structure.

3.3. Arsenate/HMO Sorption Complexes

Arsenic K-edge XANES spectra of As(V)/HMO sorption samples and the Mn(II)-arsenate precipitate are plotted in Figure 6a. The average absorption edge position of the As-XANES spectra is 11874.1 eV, verifying the presence of As(V). However, the As-XANES spectra of the sorption samples have a relatively sharp peak at ~11889 eV, whereas the spectrum of the precipitate sample has at least one additional broad peak at ~11885 eV, providing qualitative evidence for a different type of local coordination environment around As in the sorbed state.

Arsenic K-edge EXAFS spectra are dominated by one major frequency ascribed to scattering from the four oxygen atoms of the AsO_4 tetrahedron (Fig. 6b); this frequency produces the FT peak at ~1.3 Å (ncps; Fig. 6c). Arsenate/HMO sorption samples have an average R_{As-O} of 1.70 ± 0.01Å, which is slightly longer than the R_{As-O} value determined in the Mn(II)-arsenate precipitate (Table 3). This first-shell distance is consistent with AsO_3OH or $AsO_2(OH)_2$ species (Baur and Khan, 1970; Foster et al., 1998b), and is similar to R_{As-O} values determined for arsenate sorbed on hydrous iron oxide surfaces (Waychunas et al., 1993, 1995; Manceau, 1995; Fendorf et al., 1997).

To determine the structure of As(V) sorption complexes, Mn second-neighbor atoms were tested at different distances corresponding to different types of binding geometries. Because of positive correlation between the coordination number (N) and mean thermal/static disorder parameter (σ^2), the latter was fixed at 0.004 A^2, a value derived from EXAFS fits to the main Fe shell in scorodite ($FeAsO_4 \cdot 2H_2O$; Foster et al., 1998b). The decision to use a σ^2 value from the scorodite fit was made because geigerite contains two unique As positions that are superimposed in the EXAFS spectrum, leading to higher-than-normal σ^2 values for the main Mn shell in this phase (Table 3). In both Fourier-filtered and raw EXAFS fits, scattering between

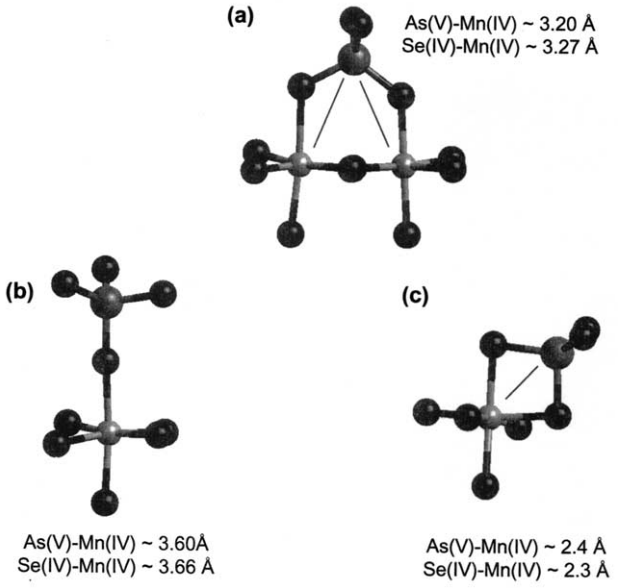

Fig. 7. Idealized geometry of As(V) sorption complexes on synthetic vernadite and K-birnessite based on sorption complex geometries proposed for As(V) adsorption on hydrous Fe(III) oxides. The sorption complexes are illustrated for As(V), but interatomic distances for Se(IV) in identical coordination are listed as well. Complex (a) is generally agreed to be the predominant complex formed by sorbed As(V) and Se(IV) on hydrous Fe(III) oxides. Idealized polyhedra ($R_{Mn\text{-}O}$ = 1.90 Å, $R_{Se\text{-}O}$ = 1.71 Å, and $R_{As\text{-}O}$ = 1.69 Å) were used to calculate the interatomic distances.

As and ~2 Mn at ~3.16 Å reproduced the majority of the amplitude of the FT peak at 2.7 Å (ncps, sorption samples; Table 3). These parameters differ substantially from the coordination of arsenate in the Mn-arsenate precipitate (in which the closest Mn atoms are at 3.46 Å; Table 3), indicating that this or a similar precipitate phase did not form during sorption experiments. Over the ranges of pH, reaction times, and As(V) sorption densities we examined, EXAFS fit parameters did not vary appreciably (Table 3). In addition, arsenate sorption complexes on K-birnessite and δ-MnO_2 appear identical by EXAFS analysis.

Models of As(V) sorption geometry that were based on EXAFS-derived interatomic distances and coordination numbers were constructed by using ideal MnO_6 octahedra with $R_{Mn\text{-}O}$ = 1.90 Å (as determined by our Mn-EXAFS analysis). The $R_{As\text{-}Mn}$ distance of ~3.16 Å obtained from EXAFS fits can be reasonably well matched by a bidentate, bridging sorption complex analogous to the type identified in previous EXAFS studies of As(V) sorption on Fe(III)-oxyhydroxides (Waychunas et al., 1993, 1995; Manceau, 1995; Fendorf et al., 1997) (Fig. 7a). The As-Mn interatomic distance can deviate from the distances shown in Figure 7 depending on the tilt of the sorption complex relative to the mineral surface and on deviations from the As-O and Mn-O distances used in these calculations.

The presence of a large proportion of monodentate, corner-sharing complexes such as illustrated in Figure 7b is improbable, because the addition of a shell of Mn atoms representing this complex did not converge on realistic values in the fit. In addition, if such a complex were present, the average As-Mn interatomic distance would be shifted to values higher than the 3.15 to 3.18 Å obtained in our fits. However, the presence of a small proportion of bidentate, edge-sharing complexes analogous to those described in As(V)-Fe(III) hydroxide systems (Manceau, 1995; Fendorf et al., 1997; Fig. 7c) is probable, because inclusion of an additional shell of Mn atoms at an initial distance of ~2.8 Å (the bidentate, edge-sharing distance in As(V)-Fe(III) hydroxide systems) results in reasonable interatomic distances (2.72 to 2.79 Å), and N values (0.3 to 0.5) for the new shell, and a reduction in the goodness-of-fit parameter. Although the $R_{As\text{-}Mn}$ values differ substantially from the geometric model of this complex shown in Figure 7c, this model might not be physically realistic because one equatorial and one axial oxygen of the FeO_6 octahedron were used as linkages to the As(V) tetrahedron instead of two equatorial oxygen atoms as was done in Manceau (1995). According to least squares fits, these edge-sharing complexes are of minor importance (contributing only ~5% to the total fit) relative to bidentate, binuclear (i.e., corner-sharing) complexes (~20% contribution to the total fit). Because it is difficult to determine if the improvement in the fit represented by the addition of an edge sharing complex is statistically significant, a shell of edge-sharing complexes were not included in the fits shown in Figure 6 and reported in Table 3.

A recent report by Manning et al. (2002) indicates that As(V) sorption complexes on synthetic MnO_2 have a characteristic $R_{As\text{-}Mn}$ of 3.22 Å. This distance is significantly longer than the average value of $R_{As\text{-}Mn}$ determined in this study (3.16 Å). We made several attempts to find a cause for the discrepancy between our average $R_{As\text{-}Mn}$ value and the one reported by Manning et al. (2002), including rechecking the validity of our phase and amplitude functions, refitting the data by using the E_o value reported in that study (11920 instead of our value of 11885), and testing the validity of our fits over different data ranges, but these tests did not result in a shift in the refined $R_{As\text{-}Mn}$ value. The 3.22-Å distance could not be "forced" to fit our EXAFS spectra.

Another possibility is that both reported distances are correct, and in both experiments the predominant sorption complex is bidentate and binuclear, but the less abundant mononuclear sorption complex is different as a result of different experimental conditions. In this scenario, minor amounts of monodentate, mononuclear sorption complexes would be present in the samples examined by Manning et al. (2002), whereas a small amount of bidentate, mononuclear complexes would be present in our study. This is not likely, however, because the difference in distance between the edge sharing complex (at 2.7 to 2.8 Å) and the corner-sharing complex (at 3.16 Å) is approximately twice as large as the estimated resolution of peaks in the FT (0.4 Å and 0.2 Å, respectively). Because the 3.22 Å distance is completely analogous with EXAFS results in As(V)/Fe oxyhydroxide systems, it is reasonable to assume that a good guess for the As-Mn distance in a hypothetical edge sharing complex should be 2.8 Å, as previously discussed. Testing linear combinations of these $R_{As\text{-}Mn}$ values, we determine that 85% of a 3.22 Å bidentate, binuclear complex and 15% of a 2.8 Å edge-sharing complex could produce the $R_{As\text{-}Mn}$ distance of 3.16 Å determined in our analysis (less of the edge-sharing complex is needed if a shorter distance of 2.75 Å is used). However, when these distances were used as initial starting points for least-squares fits to Fourier filtered or raw EXAFS spectra, the predominant shell

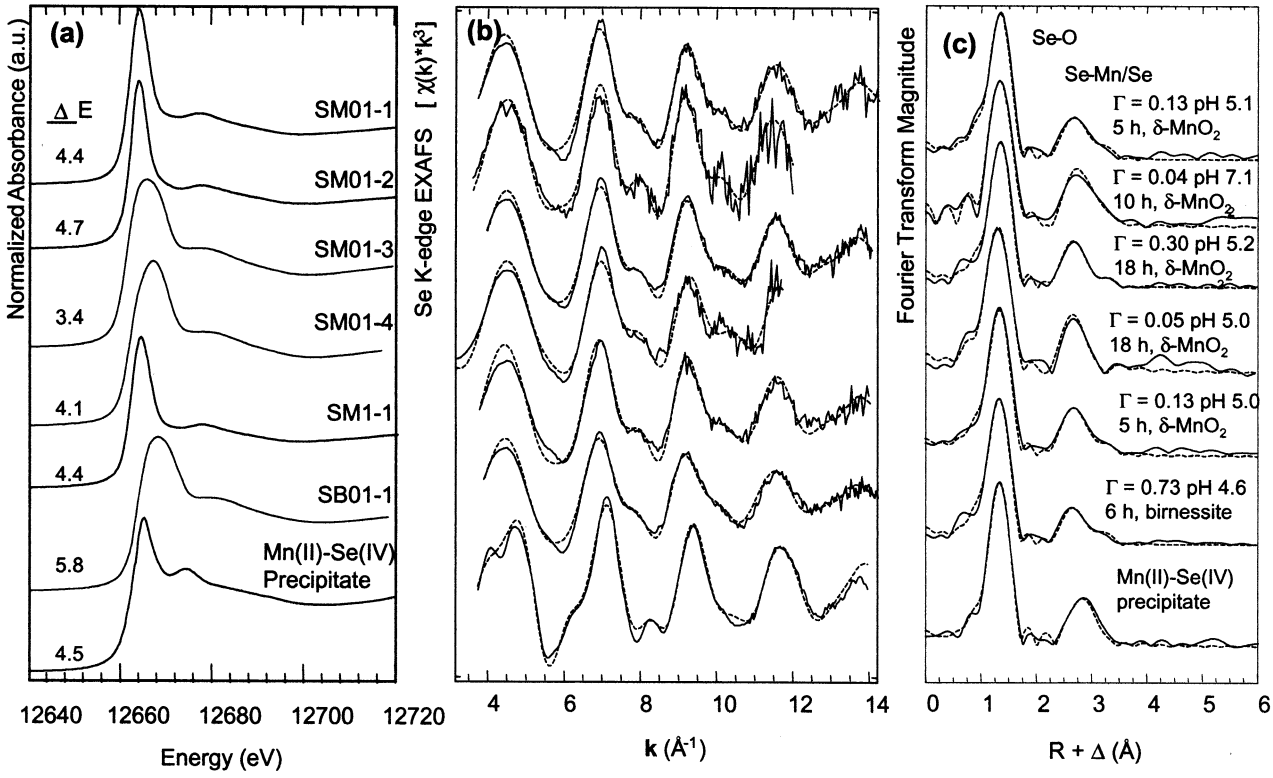

Fig. 8. (a) Normalized Se K-edge XANES spectra, (b) selenium K-edge EXAFS spectra, and (c) and Fourier transforms (solid lines) of HMO sorption samples and the Mn(II)-selenite precipitate. ΔE is the energy difference between the absorption edge position of samples/precipitates and the elemental selenium absorption edge at 12658.0 eV. XANES spectra of samples SM01-3, SM01-4, and SB01-1 were collected under low-resolution conditions and therefore have different ΔE values. Nonlinear, least-squares fits are plotted as dotted lines in (b) and (c). The precipitate EXAFS spectrum has features at ~4.1, 6.2, and 8.2 $Å^{-1}$ corresponding to one or more frequencies that are not present in the sorption sample EXAFS spectra.

always shifted back to between 3.15 to 3.18 Å. Therefore, we do not think that the shorter As-Mn distances obtained in our fits are an artifact of a combination of distances from 2 different sorption complexes.

3.4. Selenite/HMO Sorption Complexes

The absorption edge positions measured in Se(IV)/HMO Se K-edge XANES (Se-XANES) spectra indicate the predominance of Se(IV) (Fig. 8a); there was detectable selenate in only one sorption sample, which was excluded from analysis. The Se-XANES spectra of Se(IV)/HMO sorption samples are clearly different from the Se-XANES spectrum of the Mn(II)-selenite precipitate—a qualitative indication of differences in the local atomic environments.

Selenium K-edge EXAFS (Se-EXAFS) spectra of Se(IV)/HMO sorption samples are nearly identical regardless of preparation conditions or substrate, but their spectral pattern is different from the Mn(II)-selenite precipitate EXAFS spectrum, particularly at 4.7, 6.2, and 8.2 $Å^{-1}$ (Fig. 8b). These features represent a frequency that is not present in the sorption samples. We have observed high amplitude frequencies at low **k** (<5 $Å^{-1}$) such as these in several crystalline and X-ray amorphous precipitates of arsenic and selenium (Foster, 1999; and see Mn(II)-arsenate spectrum in Fig. 6b). According to FEFF7 calculations, triangular multiple-scattering paths in the selenite and arsenate oxoanions produce the majority of the amplitude of these features in crystalline precipitates such as $MnSeO_3 \cdot H_2O$ (Foster, 1999; Figs. 9a,b). The remaining amplitude of the low-**k** feature is produced by additional shells of Mn and Se atoms beyond 3.5 Å. Third, fourth, and even fifth atomic shells are not unusual in a crystalline phase as a result of its lower static disorder relative to a sorption complex. The fact that low-**k** features are missing in Se(IV)/HMO sorption sample EXAFS spectra argues against the formation of well-ordered and/or crystalline precipitates.

This distinction is important to make because fits to the EXAFS spectra of the Mn(II)-selenite precipitate and to the selenite/HMO sorption samples are very similar, and otherwise suggest that precipitation of a Mn(II)-selenite-like phase occurred during sorption of selenite on HMOs. First, the refined $R_{Se\text{-}O}$ values are identical (1.71 ± 0.02 Å), but because average Se-O bond distances in the selenite oxoanion do not vary significantly with local coordination, this result is not surprising. However, when compared with $R_{Se\text{-}O}$ values determined from EXAFS analysis of selenate crystalline compounds and sorption samples (~1.65 Å; Hayes et al., 1987; Manceau and Charlet, 1994), the $R_{Se\text{-}O}$ value obtained from our fits provides

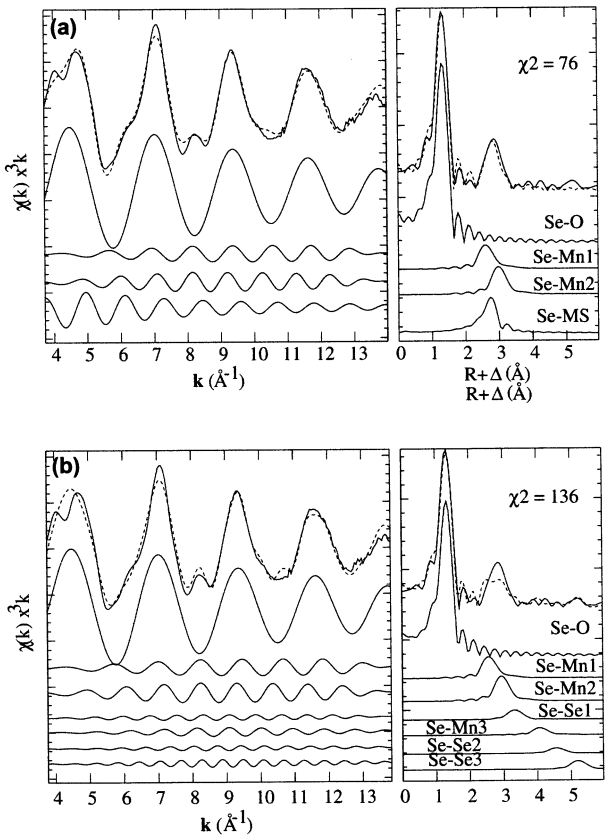

Fig. 9. Comparison of two nonlinear, least-squares fits (dotted lines) to the Mn(II)-Se(IV) precipitate EXAFS spectrum (solid lines) in which (a) a single shell of multiple scattering paths between the oxygen atoms of the selenite polyhedron is added to the basic three-shell fit and (b) and four more distant shells of Mn and Se atoms predicted from the reported structure are added to the basic three-shell fit. The former fit is considerably better than the latter.

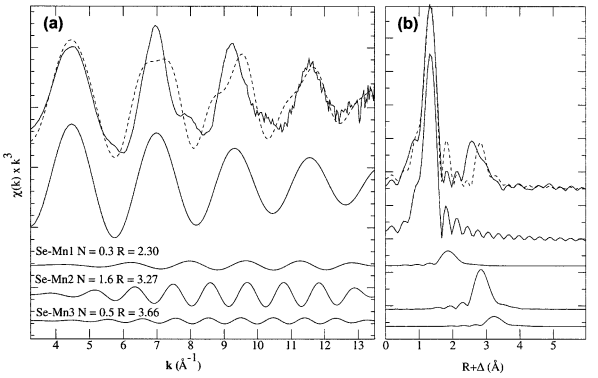

Fig. 10. Simulated EXAFS pattern (dotted line in a) and FTs (dotted line in b) of a mixture of the three hypothetical Se(IV)-Mn(IV) surface complexes illustrated in Figure 7 compared with the raw, $\mathbf{k}^3$-weighted EXAFS spectrum of sample SM01-3 (solid lines in both panels). The Se(IV)-O shell parameters used in the simulation were identical to those used in the fit to sample S4M01-3. The proportion of each species used is described in the text.

additional evidence that selenite is the predominant sorbed species on HMOs under our experimental conditions.

The important similarities between Se(IV)/HMO sorption sample fits and the Mn(II)-selenite precipitate fit are in the second- and third-shell fit parameters. The best fit to the precipitate EXAFS spectrum contains 1 Se (fixed value) at 3.03 Å and 2 Mn (fixed value) at 3.42 Å; these values are close to the interatomic distances between Se and Mn derived from the reported structure of $MnSeO_3 \cdot H_2O$ (Table 4). The number of Mn atoms in these shells (N) was fixed to values in the reported structure of $MnSeO_3 \cdot H_2O$ so that reasonable values for the mean thermal/static disorder parameter (σ^2) could be obtained for these shells by avoiding strong correlations between σ^2 and N. The σ^2 values thus obtained were used as fixed parameters in fits to Se(IV)-HMO sorption samples so that reasonable values for the number of neighboring Mn atoms could be obtained. Se(IV)-HMO sorption sample EXAFS spectra were fit best by an average of 1.6 ± 0.4 Mn at 3.07 ± 0.01 Å and 1.4 ± 0.4 Mn at 3.49 ± 0.03 Å. For both shells, the standard deviation in the fit parameters between samples is less than the estimated 99.9% (3σ) confidence values for the error of the fit parameters themselves (which varied between 0.1 to 0.8 Mn for N, and 0.01 - 0.07 Å for R; see Table 4), indicating that no major changes in sorption complex structure occurred over the range of conditions or types of sorbents examined. Hypothetical sorption complexes generated by using an average Mn-O octahedral distance of 1.90 Å (as discussed earlier in section 4.2) do not have $R_{Se\text{-}Mn}$ values concordant with EXAFS fits: corner-sharing arrangements (Figs. 7a,b) are either too long or too short to match (although introducing tilt of the polyhedra in 7b can produce $R_{Se\text{-}Mn}$ values near 3.48 Å, the second-shell Se-Mn distance), and edge-sharing complexes result in $R_{Se\text{-}Mn}$ values that are clearly too short (Fig. 7c). Although additive mixtures of the $R_{Se\text{-}Mn}$ values derived from hypothetical Se(IV)-Mn(IV) surface complexes can produce the interatomic distances derived from EXAFS fits, when a simulated EXAFS pattern is calculated on the basis of the hypothetical mixture, a poor match to the experimental spectrum is obtained. For example, an average of the Se-Mn interatomic distances of the sorption complexes illustrated in Figures 7a–c, (assuming equal proportions of each) produces an average distance of 3.08 Å, which is concordant with one of the $R_{Se\text{-}Mn}$ values derived from least-squares fits of the EXAFS data for the Se(IV)/HMO samples. Likewise, the second shell of Mn atoms derived from the same fits ($R_{Se\text{-}Mn}$ = 3.48 Å) can be matched by an average of the Se-Mn distances of the sorption complexes illustrated in Figures 7a,b (a distance of 3.46 Å is obtained). However, when these two hypothetical mixtures of sorption complexes are added together (in equal proportion) and used to construct a simulated EXAFS spectrum (using parameters for the Se-O shell from the least-squares fit of sample SM01–3), the match to sample SM01–3 is extremely poor (Fig. 10). For this reason, we believe that the two Mn shells derived from least-squares analysis do not represent combinations of other types of sorption complexes. Instead, we favor the suggestion of Banerjee and Nesbitt (2000) that there is preferential association of selenite with lower valent Mn species on HMO surfaces through adsorption, precipitation, or some combination of both, as discussed below.

The best match to the $R_{Se\text{-}Mn}$ values derived from Se(IV)/HMO samples was found in the local Se environment of $MnSeO_3 \cdot H_2O$ (Fig. 11c, Table 4), although at 3.42 Å, the

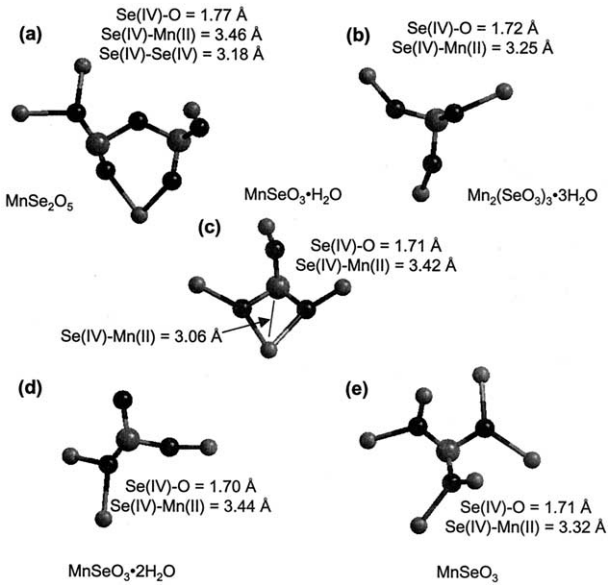

Fig. 11. Survey of selenite local environments ($<\sim$3.5 Å) in several Mn(II)-selenite crystalline phases. Characteristic bond distances and formulae are given on the figure. The large gray atoms are Se, the smaller gray atoms are Mn, and oxygen atoms are black. Coordinating oxygen atoms (except those bonded to Se(IV)) have been removed for clarity.

second Mn shell in the reported structure of $MnSeO^3 \cdot H_2O$ and in the fit to the Mn(II)-selenite precipitate is 0.07 shorter than the second shell distance in the Se(IV)-HMO sorption samples (Table 4). This match raised concern that precipitation occurred during sorption of selenite on the HMOs. As discussed in section 4.1, thermodynamic evidence suggests that precipitation should not have occurred under the conditions of our sorption experiments (Fig. 3a), and detailed comparison of the XANES and EXAFS spectra of sorption samples and the Mn(II)-selenite precipitate suggests some structural differences; however, these qualitative lines of evidence did not completely alleviate our concern that some type of nanoscale precipitate may have formed.

Selenite/vernadite sorption samples were examined by TEM to provide more direct evidence for precipitation, but definitive results were not obtained. We found no evidence for the formation of well-crystallized material; selected area diffraction yielded only ring patterns typical of poorly crystalline HMO (not shown), not spot patterns as would be expected for a well-crystallized phase such as the Mn(II)-selenite precipitate. Also, small spot size energy dispersive analysis of these samples did not yield a selenium signal. Although this technique would not be sensitive enough to detect sorbed selenite, presumably such a signal would be produced from a precipitate, which should contain Se above the approximate 5000 mg/kg detection limit.

On the basis of this analysis and evidence previously discussed, we cannot rule out the possibility of formation of nanoscale Mn(II)-selenite precipitates because of the similarity of Se(IV)-Mn(II) interatomic distances in the $MnSeO_3 \cdot H_2O$-like phase and Se(IV)-Mn interatomic distances in Se(IV) sorption complexes on HMOs. The relative amounts of Mn(III) and Mn(II) species present in the coordination environment of adsorbed or precipitated Se(IV) could not be directly assessed because of the range of Mn(III)-O bond distances produced by Jahn-Teller distortion of the $Mn(III)O_6$ octahedron [1.94 to 2.14 Å in $Mn(III)_2(SeO_3)_3 \cdot 3H_2O$; Koskenlinna and Valkonen, 1977a), which overlap those of Mn(II)-O in $MnSeO_3 \cdot H_2O$ (Table 4). However, XPS studies indicate that Mn(III) is the predominant reduced Mn species on birnessite surfaces during reaction with Se(IV) (Banerjee and Nesbitt, 2000), so Mn(III) could play an important role in Se(IV) sorption on vernadite as well. Although Se(IV)-Mn(III) distances in $Mn(III)_2(SeO_3)_3 \cdot 3H_2O$ do not match the Se(IV)-Mn distances derived from fits to the Se-EXAFS of Se(IV)-HMO sorption samples (Table 4), if a Mn(II)-Se(IV) precipitate formed during sorption it might contain substantial Mn(III) as a compositional impurity. Furthermore, if a precipitate formed during sorption of Se(IV) on the HMOs, it does not appear to be ordered beyond $\sim$3.6 Å on the basis of comparison with the Se-EXAFS of the crystalline $MnSeO_3 \cdot H_2O$-like phase examined in this study.

4. DISCUSSION

Regardless of whether Se(IV) forms true adsorption complexes with lower-valent Mn sites or nanoscale surface precipitates, our EXAFS results support the conclusion of Banerjee and Nesbitt (2000) that the substantial difference in oxidation kinetics of As(III) and Se(IV) on K-birnessite is in part related to the adsorption of Se(IV) to surface-associated Mn(II) and/or Mn(III) and subsequent reaction retardation or cessation. Although formation of Mn(II)-selenite complexes alone would definitely halt selenite oxidation, formation of Mn(III)-selenite sorption complexes alone might not. Scott (1991) calculated that the oxidation of Se(IV) by Mn(III) is thermodynamically feasible, but XPS data collected by Banerjee and Nesbitt (2000) suggest that the reaction does not proceed or is very slow relative to the rate of As(III) oxidation by Mn(III) (Chiu and Hering, 2000). Combined macroscopic uptake and spectroscopic investigations of Se(IV) sorption/oxidation on manganite [Mn(III)OOH], similar to those conducted for arsenite (Chiu and Hering, 2000), would determine the feasibility of Se(IV) oxidation by Mn(III) and provide better constraints on the relative importance of Mn(III) to Mn(II) surface species on other HMOs.

We used empirical bond valence analysis to test the plausibility of EXAFS-derived As(V) and Se(IV) sorption complex geometries on HMOs; the results are also useful for interpreting trends in the sorption of arsenic and selenium oxoanions on HMO. This analysis uses definitions and constants reported in Brown and Altermatt (1985) and Bargar et al. (1997a) along with Pauling's second rule (Pauling, 1960) applied to surface oxygen atoms to determine the favorable sites of adsorption in a given system. Although the bond valence approach in combination with EXAFS studies of Pb(II)-metal oxide systems (Bargar et al., 1997a,b) has proven useful, it should be emphasized that bond valence analysis does not provide information on the mechanisms or relative energetics of sorption reactions, nor does it account for other thermodynamic considerations that may affect the relative abundance or stability of surface complexes (Bargar et al., 1997a). Except where explicitly stated, the results discussed below employed Mn(IV)-O, Mn(III)-O (high spin), Mn(II)-O, As(III)-O, As(V)-O, Se(IV)-

Table 5. Bond valence analyses of surface functional groups on HMOs using bond lengths derived from ionic radii tables compiled by Shannon (1976), which are very similar to the EXAFS-derived lengths reported in Tables 2, 3, and 4. Charges are not assigned to surface groups with adsorbed As/Se oxoanions, since the net charge on these surface complexes will depend on the number of surface groups bonded to the oxoanion. The Mn(IV)OH group is arbitrarily assigned a charge of 0 for bookkeeping purposes.

	Sum of bond strength at oxygen (vu)		Saturation State			
Surface species	No H-bonds	With H bonds[a]	(−)	Saturated	(+)	Prediction
Mn(IV) only						
$[Mn(OH)^{0}]$[b]	1.35–1.55	1.94–2.05[c]	−	Saturated		Stable
Mn-O-As(III)	1.75	2.01		Saturated		Stable
Mn-O-As(V)	1.87	2.00–2.12		Saturated	+	Some stable
Mn-O-Se(IV)	1.98		−			Stable
Mn-O-Se(VI)	2.12				+	Unstable
Mn-(OH)-As(III)	>2.43				+	Unstable
Mn-(OH)-As(V)	≥2.54				+	Unstable
Mn-(OH)-Se(IV)	≥2.67		−		+	Unstable
Mn-(OH)-Se(VI)	≥3.00		−		+	Unstable
$[Mn(OH_2)^{+1}]$	2.03–2.43			Saturated	+	Some stable
$[Mn\text{-}O\text{-}Mn]^{0}$	1.34	≤1.84	−			Stable
$[(Mn\text{-}OH\text{-}Mn)^{+1}]$	2.02–2.22			Saturated	+	Some stable
$[(3Mn\text{-}O)^{+1}]$	2.02			Saturated	+	Stable
Mn(IV) and Mn(II)						
2Mn(IV,II)-O-As(III)[d]	1.99			Saturated	+	Stable
2Mn(IV,II)-O-As(V)	2.25				+	Unstable
2Mn(IV,II)-O-Se(IV)	2.36				+	Unstable
2Mn(IV,II)-O-Se(VI)	2.50				+	Unstable
Mn(IV) and Mn(III)						
2Mn(IV,III)-O-As(III)	>2.15				+	Unstable
2Mn(IV,III)-O-As(V)	>2.35				+	Unstable
2Mn(IV,II)-O-Se(IV)	>2.51				+	Unstable
2Mn(IV,II)-O-Se(VI)	>2.64				+	Unstable
Mn(III) and Mn(II)						
2Mn(III,II)-O-As(III)	1.80–2.04	>1.93		Saturated	+	Stable
2Mn(III,II)-O-As(V)	2.00–2.24			Saturated	+	Some stable
2Mn(III,II)-O-Se(IV)	2.05–2.29			Saturated	+	Some stable
2Mn(III,II)-O-SE(VI)	2.15–2.38				+	Unstable

[a] Denotes hydrogen bonds. The range of H bond strengths from neighboring water atoms is 0.13– 0.25 valence units (vu) from Bargar et al. (1997a). The maximum coordination number of oxygen atoms is assumed to be 4.

[b] Brackets denote surface functional groups.

[c] The range of bond valences for hydroxyl bonds is $0.68 \leq sOH \leq 0.88$ v.u. Bargar et al., 1997a).

[d] This shorthand denotes an oxygen atom bonded to two Mn atoms: in this case, one is Mn(IV), and the other is Mn(II). The ionic radii used in bond strength calculations were derived from tables compiled by Shannon (1976). We used the following Mn-O bond distances in the bond strength calculations: Mn(II)-O = 2.15, Mn(III)-O = 1.93 Å (high spin, undistorted), Mn(IV)-O = 1.90 Å, As(III)-O = 1.76 Å, As(V)-O = 1.70 Å, Se(IV)-O = 1.71 Å, and Se(VI)-O = 1.65 Å.

O, and Se(VI)-O distances from crystal structure reports or EXAFS analyses from this study or from Foster (1999).

Six predictions can be drawn from the bond valence results collected in Table 5: (1) As(III), As(V), and Se(IV) oxoanion sorption complexes that contain singly coordinated surface oxygen atoms bound to Mn(II), Mn(III), or Mn(IV) should be stable; (2) As or Se oxoanion surface complexes that contain surface hydroxyl groups should be unstable, regardless of the oxidation state of the Mn atom to which the hydroxyl is bonded; (3) Surface complexes between Se(VI) oxoanions and [Mn(IV)-O] surface functional groups should be unstable; (4) As and Se oxoanions should not exchange for bridging oxygen atoms in [Mn(IV)-O-Mn(IV)] and [Mn(III)-O-Mn(IV)] surface functional groups; (5) As(III) oxoanions should form stable bonds with [Mn(II)-O-(Mn(IV)] functional groups, but the analogous complexes with As(V), Se(IV), and Se(VI) should be unstable; and (6), with the exception of Se(VI), [Mn(II)-O-Mn(III)] functional groups should form stable complexes with As and Se oxoanions.

These predictions are useful for interpreting our EXAFS results and the results of previous studies but do not provide absolute constraints. For example, the proposed predominant sorption complex geometry of As(V) on HMOs (Fig. 7a) is predicted to be stable by bond valence analysis, but so are the other two hypothetical sorption complexes shown in Figure 7. Prediction (3) is consistent with macroscopic uptake studies indicating that selenate sorbs very weakly to HMOs (Balistrieri and Chao, 1990). However, if the actual range of Mn(IV)-O distances in K-birnessite and todorokite (a crystalline tectomanganate model for vernadite) are considered (1.81 to 2.05 Å), Se(VI) is predicted to form stable sorption complexes with [Mn(IV)-O] surface functional groups having an Mn-O bond length greater than 1.95 Å. Prediction (5) suggests that a greater variety of HMO surface sites are amenable to As(III) sorption than to As(V) sorption. This constraint may provide a rationale for understanding why As(III) appears to effectively outcompete As(V) for sorption sites on HMOs, leading to near-stoichiometric release of the otherwise strongly sorbing As(V) to solution during As(III) oxidation (Scott and Morgan, 1995).

5. CONCLUSIONS

In the absence of arsenite, the predominant arsenate sorption complex on synthetic K-birnessite and vernadite has 2.0 ± 0.4 neighboring Mn atoms at 3.16 ± 0.01 Å, suggesting that adsorption occurs primarily to Mn(IV) sites on HMOs. Coordination parameters derived from nonlinear, least-squares fits to raw EXAFS spectra are consistent with a bidentate bridging coordination geometry analogous to previous spectroscopic studies of As(V) sorption on ferric hydroxides. Results from the Se(IV)/HMO system do not provide conclusive evidence for or against the formation of nanoscale Mn(II)-Se(IV) precipitates during sorption experiments. Fits to EXAFS spectra indicate a coordination environment of 1.6 ± 0.4 Mn at 3.07 ± 0.01 Å and 1.4 ± 0.4 Mn at 3.49 ± 0.03 Å around Se(IV) in the HMO sorption samples. These parameters are very similar to those derived from EXAFS analysis of a crystalline Mn(II)-Se(IV) precipitate. However, clear differences in the XANES and EXAFS spectra indicate that the coordination environment of Se and/or the degree of atomic ordering in the HMO sorption samples is different from that in the crystalline Mn(II)-selenite precipitate. Whichever the case, the results of this study point to a significant interaction between lower-valent Mn and Se(IV) oxoanions on HMOs that appears to be less important in As(V)/HMO systems, in which reductive dissolution of the Mn surface does not occur.

Acknowledgments— Portions of this research were carried out at the Stanford Synchrotron Radiation Laboratory, a national user facility operated by Stanford University on behalf of the U.S. Department of Energy, Office of Basic Energy Sciences. SSRL is supported by the Department of Energy, Office of Biologic and Environmental Research, and by the National Institutes of Health, National Center for Research Resources, Biomedical Technology Program. This work was supported by the Department of Energy through grant DE-FG03-93ER14347-A008, by the National Science Foundation through NSF grant CHE-0089215, and by the Corning Foundation Graduate Science Fellowship program. TEM studies were performed at the National Center for Electron Microscopy (NCEM), Lawrence Berkeley National Laboratory, Berkeley, California, and we gratefully acknowledge Chuck Echer of the NCEM for assistance. We thank H. W. Nesbitt (University of Western Ontario), two anonymous referees, and GCA associate editor P. A. O'Day for constructive reviews of the manuscript.

Associate editor: P. A. O'Day

REFERENCES

Balistrieri L. S. and Murray J. W. (1982) The surface chemistry of δ-MnO_2 in major ion seawater. *Geochim. Cosmochim. Acta* **46,** 1041–1052.

Balistrieri L. S. and Chao T. T. (1990) Adsorption of selenium by amorphous iron oxyhydroxide and manganese dioxide. *Geochim. Cosmochim. Acta* **54,** 739–751.

Banerjee D. and Nesbitt H. W. (2000) XPS study of reductive dissolution of birnessite by H_2SeO_3 with constraint on reaction mechanism. *Am. Mineral.* **85,** 817–825.

Bargar J. R., Brown G. E. Jr., and Parks G. A. (1997a) Surface complexation of Pb(II) at oxide-water interfaces: I. XAFS and bond-valence determination of mononuclear and polynulcear Pb(II) sorption products and aluminum oxides. *Geochim. Cosmochim. Acta* **61,** 2617–2637.

Bargar J. R., Brown G. E. Jr., and Parks G. A. (1997b) Surface complexation of Pb(II) at oxide-water interfaces: II. XAFS and bond-valence determination of mononuclear and polynulcear Pb(II) sorption products and surface functional groups on iron oxides. *Geochim. Cosmochim. Acta* **61,** 2639–2652.

Baur W. H. and Khan A. A. (1970) On the crystal chemistry of salt hydrates. VI. The crystal structures of disodium hydrogen orthoarsenate heptahydrate and disodium hydrogen orthophosphate heptahydrate. *Acta Cryst.* **B26,** 1584–1596.

Brown I. D. and Altermatt D. (1985) Bond-valence parameters obtained from a systematic analysis of the inorganic crystal structure database. *Acta Cryst.* **B41,** 244–247.

Burns R. G. and Burns V. M. (1979) Manganese oxides. In *Marine Minerals* (ed. P. H. Ribbe), pp. 1–46. Mineralogical Society of America.

Catti M. and Franchini-Angela M. (1979) Krautite, $Mn(H_2O)(AsO_3OH)$: Crystal structure, hydrogen bonding, and relations with haidingerite and pharmacolite. *Am. Mineral.* **64,** 1248–1254.

Chiu V. Q. and Hering J. G. (2000) Arsenic adsorption and oxidation at manganite surfaces. 1. Method for simultaneous determination of adsorbed and dissolved arsenic species. *Environ. Sci. Technol.* **34,** 2029–2034.

Chukhrov F. V., Dritts V. A., Gorshkov A. I., Sakharov B. A., and Dikov Y. P. (1987) Structural models of vernadite. *Int. Geol. Rev.* **29,** 1337–1347.

Drits V. A., Silvester E., Gorshkov A. I., and Manceau A. (1997) Structure of synthetic monoclinic Na-rich birnessite and hexagonal birnessite: I. Results from X-ray diffraction and selected-area electron diffraction. *Am. Mineral.* **82,** 946–961.

Fendorf S. E., Eick M. J., Grossl P., and Sparks D. L. (1997) Arsenate and chromate retention mechanisms on goethite. 1. Surface structure. *Environ. Sci. Technol.* **31,** 315–326.

Foster A. L. (1999) Partitioning and transformation of arsenic and selenium in natural and laboratory systems. Ph.D. thesis. Stanford University.

Foster A. L., Brown G. E. Jr., and Parks G. A. (1998a) X-ray absorption fine-structure spectroscopy study of photocatalyzed, heterogeneous As(III) oxidation on kaolin and anatase. *Environ. Sci. Technol.* **32,** 1444–1452.

Foster A. L., Brown G. E. Jr., Parks G. A., and Tingle T. N. (1998b) Quantitative speciation of arsenic in mine tailings using X-ray absorption spectroscopy. *Am. Mineral.* **89,** 553–568.

Fritsch S., Post J. E., and Navrotsky A. (1997) Energetics of low-temperature polymorphs of manganese dioxide and oxyhydroxide. *Geochim. Cosmochim. Acta* **61,** 2613–2616.

Gabrielson O. (1951) Manganiferous hoernesite and manganese-hoernesite from Långban, Sweden. *Arkiv. Mineral. Geol.* **1,** 333–337.

George G. G. and Pickering I. J. (1992) *EXAFSPAK: A Suite of Computer Programs for Analysis of X-Ray Absorption Spectra*. Stanford Synchrotron Radiation Laboratory.

Graeser S., Schwander H., Bianchi R., Pilati T., and Gramaccioli C. (1989) Geigerite, the Mn analog of chudobaite: Its description and crystal structure. *Am. Mineral.* **74,** 676–684.

Hayes K. F., Roe A. L., Brown G. E. Jr., Hodgson K. O., Leckie J. O., and Parks G. A. (1987) In situ X-ray absorption study of surface complexes: Selenium oxoanions on α-FeOOH. *Science* **238,** 783–786.

Hess R. E. and Blanchar R. W. (1976) Arsenic stability in contaminated soils. *Soil Sci. Soc. Am. J.* **40,** 847–852.

Koskenlinna M., Niinistö L., and Valkonen J. (1976) Manganese selenite dihydrate, $MnSeO_3 \cdot 2H_2O$. *Cryst. Struct. Commun.* **5,** 663–666.

Koskenlinna M. and Valkonen J. (1977a) Jahn-Teller distortions in the structure of manganese(III) selenite trihydrate, $Mn_2(SeO_3)_3 \cdot 3H_2O$.. *Acta Chem. Scand. A* **31,** 611–614.

Koskenlinna M. and Valkonen J. (1977b) The crystal structure of manganese(II) selenite monoduterate. *Acta Chem. Scand. A* **31,** 752–754.

Kunzendorf H. and Glasby G. P. (1992) Tungsten accumulation in Pacific ferromanganese deposits. *Mineral. Deposita* **27,** 147–152.

La Force M. J., Hansel C. M., and Fendorf S. E. (2000) Arsenic speciation, seasonal transformations, and co-distribution with iron in a mine waste-influenced palustrine emergent wetland. *Environ. Sci. Technol.* **34,** 3937–3943.

Manceau A. (1995) The mechanism of anion adsorption on iron oxides: Evidence for the binding of arsenate tetrahedra on free $Fe(O,OH)_6$ edges. *Geochim. Cosmochim. Acta* **59,** 3647–3653.

Manceau A., Gorshkov A. I., and Drits V. A. (1992a) Structural chemistry of Mn, Fe, Co, and Ni in manganese hydrous oxides: Part I. Information from XANES spectroscopy. *Am. Mineral.* **77,** 1133–1143.

Manceau A., Gorshkov A. I., and Drits V. A. (1992b) Structural chemistry of Mn, Fe, Co, and Ni in manganese hydrous oxides: Part II. Information from EXAFS spectroscopy and electron and X-ray diffraction. *Am. Mineral.* **77,** 1144–1157.

Manceau A. and Charlet L. (1994) The mechanism of selenate adsorption on goethite and hydrous ferric oxide. *J. Colloid Interf. Sci.* **168,** 87–93.

Manning B. A., Fendorf S. E., Bostick B., and Suarez D. L. (2002) Arsenic(III) oxidation and arsenic(V) adsorption reactions on synthetic birnessite. *Environ. Sci. Technol.* **36,** 976–981.

Mayland H. F. (1994) Selenium in plant and animal nutrition. In *Selenium in the Environment* (eds. W. T. Frankenberger and S. Benson), pp. 29–67. Marcel Dekker.

McKenzie R. M. (1971) The synthesis of birnessite, cryptomelane, and some other oxides and hydroxides of manganese. *Mineral. Mag.* **38,** 493–502.

McKenzie R. M. (1981) The surface charge on manganese dioxides. *Aust. J. Soil Res.* **19,** 41–50.

McKenzie R. M. (1989) Manganese oxides and hydoxides. In *Minerals in Soil Environments* (eds. J. B. Dixon and S. B. Weed), pp. 439–465. Soil Science Society of America.

Morgan J. J. and Stumm W. (1964) Colloid-chemical properties of manganese dioxide. *J. Colloid Sci.* **19,** 347–359.

Nesbitt H. W., Canning G. W., and Bancroft G. M. (1998) XPS study of reductive dissolution of 7-Å birnessite by H_3AsO_3, with constraints on reaction mechanism. *Geochim. Cosmochim. Acta* **62,** 2097–2110.

O'Day P. A., Chisholm-Brause C. J., Towle S. N., Parks G. A., and Brown G. E. Jr (1996) . X-ray absorption spectroscopy of Co(II) sorption complexes on quartz (α-SiO_2) and rutile (TiO_2). *Geochim. Cosmochim. Acta* **60,** 2515–2532.

Oscarson D. W., Huang P. M., and Liaw W. K. (1981) Role of manganese in the oxidation of arsenite by freshwater lake sediments. *Clays Clay Miner.* **29,** 219–225.

Pandya K. I. (1994) Multiple-scattering effects in X-ray absorption fine structure: Chromium in a tetrahedral configuration. *Phys. Rev. B* **50,** 15509–15515.

Parker D. R., Zelazny L. W., and Kinraide T. B. (1987) Improvements to the program GEOCHEM. *Soil Sci. Soc. Am. J.* **51,** 488–491.

Pauling L. (1960) *The Nature of the Chemical Bond*. Cornell University Press.

Post J. E. and Bish D. L. (1988) Rietveld refinement of the todorokite structure. *Am. Mineral.* **73,** 861–869.

Post J. E. and Veblen D. R. (1990) Crystal structure determination of synthetic sodium, magnesium, and potassium birnessite using TEM and the Rietveld method. *Am. Mineral.* **75,** 477–489.

Ressler T. (1998) WinXAS: A program for X-ray absorption spectroscopy data analysis under MS-Windows. *J. Synchrotron Rad.* **5,** 118–122.

Ressler T., Brock S. L., Wong J., and Suib S. L. (1999) Multiple-scattering EXAFS analysis of tetraalkylammonium manganese oxide colloids. *J. Phys. Chem. B* **103,** 6407–6420.

Rochette E. A., Li G. C., and Fendorf S. E. (1998) Stability of arsenate minerals in soil under biotically-generated reducing conditions. *Soil Sci. Soc. Am. J.* **62,** 1530–1537.

Roman-Ross G., Tournassat C., and Charlet L. (2001) The As-MnO_2 redox reaction: Coal-mine lake geochemistry and experimental studies. *Eos. Trans. AGU* Spring Mtg. Suppl. 82, 5206.

Sadiq M. (1997) Arsenic chemistry in soils: An overview of thermodynamic predictions and field observations. *Water Air Soil Poll.* **93,** 117–136.

Savage K. S., Tingle T. N., O'Day P. A., Waychunas G. A., and Bird D. K. (2000) Arsenic speciation in pyrite and secondary weathering phases, Mother Lode Gold District, Tuolumne County, California. *Appl. Geochem.* **15,** 1219–1244.

Scott M. J. (1991) Kinetics of adsorption and redox processes on iron and manganese oxides: Reactions of As(III) and Se(IV) at goethite and birnessite surfaces. Ph.D. thesis. California Institute of Technology.

Scott M. J. and Morgan J. J. (1995) Reactions at oxide surfaces. 1. Oxidation of As(III) by synthetic birnessite. *Environ. Sci. Technol.* **29,** 1898–1905.

Scott M. J. and Morgan J. J. (1996) Reactions at oxide surfaces. 2. Oxidation of Se(IV) by synthetic birnessite. *Environ. Sci. Technol.* **30,** 1990–1996.

Shannon R. D. (1976) Revised effective ionic radii and systematic studies of interatomic distances in halides and chalcogenides. *Acta Cryst.* **A32,** 751–767.

Sillén L. G., Martell A. E. (1964) Stability Constants of Metal-Ion Complexes. Section I: Inorganic Ligands. Chemical Society, London.

Smedley P. L. Kinniburgh D. G. Huq I., Zhen-dong L., and Nicolli H. B. (2001) International perspectives on naturally occurring arsenic problems in groundwater. In *Arsenic Exposure and Health Effects IV* (eds. W. R. Chappell, C. O. Abernathy, and R. L. Calderon), pp. 9–26. Elsevier.

Stern E. A. (1993) The number of relevant independent points in X-ray absorption fine-structure spectra. *Phys. Rev. B* **48,** 9825–9827.

Takamatsu T., Kawashima M., and Koyama M. (1985) The role of Mn^{2+}-rich hydrous manganese oxide in the accumulation of arsenic in lake sediments. *Water Res.* **19,** 1029–1032.

Takematsu, N. Sato, Y. Okabe, S. Usui A. (1990) Uptake of selenate and other oxoanionic elements in marine ferromanganese concretions of different origins. *Mar. Chem.* 31271–283.

Teo, B. K. (1986) *EXAFS: Basic Principles and Data Analysis*. Springer-Verlag.

Turner S. and Buseck P. (1979) Manganese oxide structures and their intergrowths. *Science* **203,** 456–458.

Waychunas G. A., Rea B. A., Fuller C. C., and Davis J. A. (1993) Surface chemistry of ferrihydrite: Part 1. EXAFS studies of the geometry of coprecipitated and adsorbed arsenate. *Geochim. Cosmochim. Acta* **57,** 2251–2269.

Waychunas G. A., Davis J. A., and Fuller C. C. (1995) Geometry of sorbed arsenate on ferrihydrite and crystalline FeOOH: Re-evaluation of EXAFS results and topological factors in predicting sorbate geometry, and evidence for monodentate complexes. *Geochim. Cosmochim. Acta* **59,** 3655–3661.

Yamauchi H. and Fowler B. A. (1994) Toxicity and metabolism of inorganic and methylated arsenicals. In *Arsenic in the Environment, Part 2: Human Health and Ecosystem Effects* (ed. J. O. Nriagu). Wiley. p. 35–53.

Zabinsky S. I., Rehr J. J., Ankudinov A., Albers R. C., and Eller M. J. (1995) Multiple scattering calculation of X-ray absorption spectra. *Phys. Rev. B* **52,** 2995–3009.